

OPTOMECHANICS AS A PROBE FOR NEW PHYSICS:
FROM DARK MATTER TO SPONTANEOUS WAVE FUNCTION COLLAPSE

by

Utkal Pandurangi

A Thesis Submitted to the Faculty of the

JAMES C. WYANT COLLEGE OF OPTICAL SCIENCES

In Partial Fulfillment of the Requirements

For the Degree of

MASTER OF SCIENCE

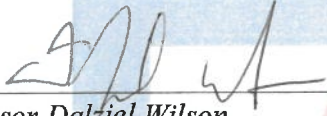
In the Graduate College

THE UNIVERSITY OF ARIZONA

2022

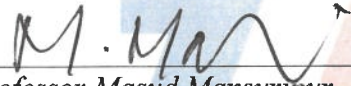
THE UNIVERSITY OF ARIZONA
GRADUATE COLLEGE

As members of the Master's Committee, we certify that we have read the thesis prepared by **Utkal Pandurangi**, titled *Optomechanics as a Probe for New Physics: From Dark Matter to Spontaneous Wave Function Collapse* and recommend that it be accepted as fulfilling the thesis requirement for the Master's Degree.



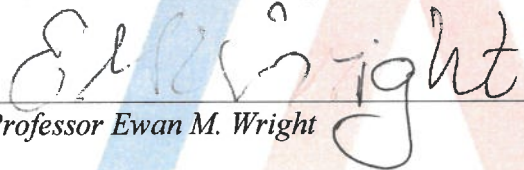
Professor Dalziel Wilson

Date: 8/19/22



Professor Masud Mansuripur

Date: 8/19/2022



Professor Ewan M. Wright

Date: 8/19/22

Final approval and acceptance of this thesis is contingent upon the candidate's submission of the final copies of the thesis to the Graduate College.

I hereby certify that I have read this thesis prepared under my direction and recommend that it be accepted as fulfilling the Master's requirement.



Professor Dalziel Wilson
Master's Thesis Committee Chair
Wyant College of Optical Sciences

Date: 8/19/22

ARIZONA

Acknowledgments

Dalziel Wilson; It's hard to find advisors like you, who can bear slow progress and countless questions. Despite me not being qualified and a good fit for our group, you always stood by me; with grace, a smile, and patience, *immense* patience. You have taught me so many important lessons of scientific inquiry and presentation, often from scratch and by sweet spoon-feeding. As someone who leads by example, you have set a healthy research culture in our group, of which I am very proud to be a small part. You have also exponentially improved the quality of my thesis and defense, whose most content-and-narrative you directly or indirectly influenced. I feel very fortunate to have got so much one-on-one discussion time with someone so well-qualified and busy as you. You always cared about me, even if that was of no concern to you or your research group, and for that, I am ever-grateful.

Aman Agrawal; it has been the most amazing experience to be your 672-labmate and your little brother. I have learned a ton about research and life-in-general, just by talking with you and observing the way you go about your stuff. *Mitul Chowdhury*; I have been fortunate to have spent time with someone like you, who is filled with so much knowledge, wit, kindness, and some more knowledge. *Christian Pluchar*; the way you manage your work-life inspires and I thank you for all the advice and support you give me as my senior. *Charles Condos*; your journey into physics and your day-to-day work have motivated me. *Bre' Anna Sherman* and *John Omnik*; thank you for the sweet summer of 2021, where we ate food, played ping-pong, and talked food. I thank *Jack Manley*, *Atkin Hyatt*, and *Tyler Nelson* and wish them the best of luck with their future. A considerable content of my thesis and defense was extensions, repetitions, or featured work done by *Dal* and our team. I owe a debt of gratitude to each one of them.

Masud Mansuripur and *Ewan Wright*; it's my great privilege to call you my thesis committee members,₂ Thank you for making it despite

your tight schedules. *Masud*, if I can aim to achieve half of your clarity in physics and math in my lifetime, I will be a content student of the art.

A big, fat thank you to *everyone* in the *Wyant College* for making *Meinel* the perfect home for us optics-peeps to shine. A special shout-out to my *Optica* soccer gang: "*OSC, OSC, OSC...*". *Brian Anderson, Jini Kandyil, and co.*: You let someone who failed 22 courses in his undergrad. study in the biggest optics mecca in the USA. Thank you for that belief. *Brian*, your kindness has inspired but also spoilt me, and I promise to get better at OPTI 570 soon. *Mark Rodriguez, and co.*, thank you for the kind and unexpected cash treats.

Thank you, *Vidya Athya*, for being my first teacher in “The American Dream” and for helping me to start off in Tucson. Thank you, *Osman Syed* and *Abinash Das*, for providing me with a cozy home in Tucson as I kept delaying my MS defense.

To all my *friends* and *family* in India, I am sorry for not keeping in touch. However, know that you were always with me in my heart as I carried out my MS program and that often carried me forward. Thank you and I love you more than you believe.

Dr. Bashi and *Dr. Shalini*, thank you for making my mind happy and strong, ready to take on life and her games.

I am incredibly fortunate to have bumped into kind and inspiring teachers and professors, for many years now. Thank you, *Ullas Agarwal*, for being that physics teacher I dreamt of growing up into; *Anith Nelleri*, for paving my optics destiny; *Lokesh Reddy*, for teaching me my first optics experiment; *Prakash Subramanian* and *Chitra Krishnan*, for introducing me to research.

Lastly, but most importantly, I am very grateful to my superwoman-*Ma*, my hero-*Pa*, my twinnie-*Dolly*, and my angel-*Dadi*, for making sure my smile never fades.

To Ma and Pa, whose many sacrifices built a life of dreams for me.

Abstract

The multi-disciplinary field of optomechanics deals with the coupling between electromagnetic radiation and mechanical motion. We discuss how optomechanical systems can be used to investigate dark matter and spontaneous wave function collapse, by setting bounds on the parameters that constitute these theories. Specifically, we focus on optomechanical systems based on silicon nitride membranes and torsion micropendula. Our table-top experiments are cost-effective and compact as compared to accelerator-based particle physics experiments.

Searching for dark matter with an optomechanical system: Dark matter (DM) is predicted to make up around eighty-five percent of the matter in our universe; however, its physical nature is unknown, spurring calls for new types of detection methods. Our approach is based on the study of nanomembrane oscillations, which might be driven by a vector “dark photon” field, similar to an electromagnetic field. However, the dark photon field exerts a force on atoms proportional to their neutron-number. Expressions for our membrane’s sensitivity to the dark photon field are derived in this thesis. Specifically, by modeling the DM signal as a Lorentzian noise peak and equating the DM spectrum with the measurement noise, we obtain lower bounds of the DM coupling strength. A key consideration is that since the DM field is uniform over the length scales of a lab, we need to monitor the membrane’s motion relative to an object with a different neutron-number. We explore a “Trampoline-on-Membrane” (TOM) device, fabricated in our laboratory, that enables this functionalization.

Testing spontaneous wave function collapse models with an optomechanical system: Spontaneous wave function collapse models are proposed to account for deviations from standard quantum mechanics and explain why quantum measurements always produce definite outcomes—rather than a superposition as predicted by the Schrödinger equation. Collapse models are typically based₅ on the inclusion of phenomenologi-

cal and non-linear terms in the Schrödinger equation, which describe the collapse of the wave function in space. Experimentally, they might manifest as accelerated decoherence of pure states made of a large number of atoms, or an excess of zero-point motion in a solid state mechanical resonator, both of which can be tested with optomechanical systems. We interpret the displacement sensitivity of our lab’s TOM device and torsional micropendulum as constraints on the Continuous Spontaneous Localization (CSL) model—the most widely studied collapse model.

The DM and CSL constraints predicted in this thesis are competitive with leading constraints set by the Laser Interferometer Gravitational-Wave Observatory (LIGO), the Laser Interferometer Space Antenna (LISA) Pathfinder, and the Eöt-Wash torsion balance experiment. We envision setting more stringent bounds in the future by operating our experiments in a cryostat.

TABLE OF CONTENTS

CHAPTER 1. INTRODUCTION	9
1.1. Signal Processing:	11
1.1.1. Autocorrelation and power spectral density (PSD):	11
1.1.2. Superposition of signals in the time domain and frequency domain:	12
1.2. Cavity optomechanical coupling	13
1.3. Optomechanical measurement: Linear response model . .	15
1.3.1. Measurement sensitivity in the frequency domain .	16
1.4. Sources of noise:	17
1.4.1. Thermal noise:	17
1.4.2. Photon shot noise (imprecision and backaction) . .	19
1.4.3. Imprecision shot noise	19
1.4.4. Radiation pressure shot noise	20
CHAPTER 2. DARK MATTER AND ITS DETECTION	21
2.1. Ultralight dark matter: phenomenology	21
2.2. Introducing the vector DM force and acceleration:	23
2.3. A mechanical dimer for detecting dark matter:	25
2.3.1. Some points to note on our dimer system’s analysis:	29
2.4. Measurement noise in dimer-based dark matter detector: .	31
2.5. Improving resolution by time averaging	33
2.6. Experimental apparatus for DM detection:	35
2.6.1. Trampoline-on-membrane (TOM) accelerometer . .	36
CHAPTER 3. COLLAPSE MODELS AND THEIR DETECTION . . .	39
3.1. Spontaneous wave function collapse models:	39
3.2. The continuous spontaneous localization (CSL) model . .	40
3.3. CSL-induced forces and torques:	42
3.3.1. CSL momentum diffusion:	42
3.3.2. CSL-induced force on a nanomembrane:	43

TABLE OF CONTENTS—*Continued*

3.3.3. CSL-induced torque on a torsion paddle:	44
3.3.4. Torsion pendulum as a torque sensor:	45
3.3.5. Measurement sensitivity in the frequency domain: .	46
3.3.6. Thermal-Noise-Limited CSL constraints	48
3.3.7. Torsion micropendulum device	49
CHAPTER 4. RESULTS AND DISCUSSION	51
CHAPTER 5. CONCLUSION AND OUTLOOK	54
BIBLIOGRAPHY	55

Chapter 1

INTRODUCTION

Cavity optomechanics [1] is the study of the interaction between light and mechanical motion, enhanced by coupling a mechanical resonator to an optical cavity. In recent years, state-of-the-art fabrication methods leading to ultra-low-loss nanomechanical resonators have generated tremendous interest in this field. Fundamental optomechanics research includes exploring the quantum limits of measurement [2] and radiation pressure-based feedback cooling [3]. Applications include acceleration and force sensing (although the chip-scale packaging capabilities of OM sensors have not yet reached the sophistication seen in microelectromechanical systems). Optomechanical (OM) systems can also form part of hybrid quantum systems—for example a nanomechanical resonator can be used to coherently couple microwave and optical photons, enabling extraction of information from cryogenic quantum computer onto a room temperature optical fiber.

The following are some favorable features of optomechanical systems:

- **High displacement and force sensitivity:** Optical fields can be quantum-noise-limited at room temperature, enabling interferometric displacement measurement with sensitivity at the femtometer level, sufficient to resolve the thermal (Brownian) motion of nanomechanical resonators. The force equivalent thermal motion of a high- Q nanomechanical resonator can moreover be as low as zeptonewtons [4]; as such, cavity optomechanical systems can be used to realize ultrasensitive force measurements.
- **High bandwidth:** Owing to the high speed of light, optical fields are sensitive to rapid perturbations, enabling displacement/force measurements with gigahertz (or higher) bandwidth. We can more-

over modulate the frequency and amplitude of optical fields at these frequencies, enabling sophisticated optical readout and control protocols.

- **Sensitivity beyond the quantum limit:** Displacement produced by radiation pressure in a optomechanical system leads to coupling of the amplitude and phase of the optical field. This intrinsic optomechanical Kerr nonlinearity can be used to squeeze the optical field, enabling displacement (and thereby, force) measurements beyond the Standard Quantum Limit [1].
- **Customizable optics:** Cavity OM coupling is produced when the resonance frequency of an optical cavity is coupled to the motion of a mechanical element. This coupling can be realized in a diversity of geometries, varying from macroscopic Fabry-Perot cavities to chip-scale microtoroidal resonators.
- **Customizable mechanics:** Likewise, mechanical resonators can be realized in a vast diversity of sizes/geometries, and functionalized to be coupled to a diversity of force fields in addition to radiation pressure, from magnetic fields to charge. This feature has led cavity optomechanical systems to be considered as “universal” transducers.

OM systems have been used to observe manifestations of the Heisenberg Uncertainty Principle (see Sec. 1.4.4) and they are increasingly being used to observe other quantum phenomena in macroscale systems. For example, OM experiments are being used to project signatures of superpositions of states of massive objects and are thus considered to be strong candidates for experimentally verifying quantum gravity.

Strained nanomechanical resonators have been shown to exhibit very high quality-factors due to a phenomenon known as dissipation dilution. Recently, it has been shown that [5] torsion modes can experience massive dissipation dilution too, like transverse flexural modes. This is expected to open the floodgates to further research in high-Q torsional optomechanics and torsional dissipation dilution.

Gravitational wave detection can also be placed under the umbrella of optomechanics. In fact, LIGO (Laser Interferometer Gravitational-Wave Observatory) and the techniques to carry out such experiments, like precision interferometry, have played a major part to spur OM research. Today, apart from gravitational waves, there are other physical theories that are being put to test by OM setups, by pursuing the detection of fundamental forces, originating from dark matter, spontaneous wave function collapse, etc.

1.1 Signal Processing:

This thesis will make heavy use of linear response theory applied to stochastic (noise) signals. Here, we provide an essential description of the power spectral density, a statistical property of noise signals that is central to our treatment of optomechanical systems.

1.1.1 Autocorrelation and power spectral density (PSD):

The autocorrelation of a signal, $x(t)$, is defined by:

$$\langle x(t)x(t + \tau) \rangle = \lim_{T \rightarrow \infty} \int_{-T/2}^{T/2} x(t)x(t + \tau) dt \quad (1.1)$$

According to the Wiener-Khinchin theorem, the Fourier transform of the autocorrelation of $x(t)$ yields the "double-sided" power spectral density:

$$S_{xx}(\omega) \equiv \int_{-\infty}^{\infty} \langle x(t)x(t + \tau) \rangle e^{-i\omega\tau} d\tau \quad (1.2a)$$

$$\propto |x(\omega)|^2 \quad (1.2b)$$

where $x(\omega)$ is the Fourier transform of $x(t)$ and

$$\langle x^2(t) \rangle = \int_{-\infty}^{\infty} S_{xx}(\omega) d\omega / 2\pi. \quad (1.3)$$

If $x(t)$ is real-valued, then $S_{xx}(\omega) = S_{xx}(-\omega)$. This motivates the definition of the "single-sided" power spectral density:

$$S_x(\omega) \equiv 2S_{xx}(\omega), \quad (1.4)$$

on the domain of $\omega > 0$, where:

$$\langle x^2(t) \rangle = \int_0^\infty S_x(\omega) d\omega / 2\pi. \quad (1.5)$$

1.1.2 Superposition of signals in the time domain and frequency domain:

Throughout this thesis, we will often jump between the time and frequency domain as we add different signals, e.g.

$$A(t) = B(t) + C(t) \rightarrow S_{AA}(\omega) = S_{BB}(\omega) + S_{CC}(\omega), \quad (1.6)$$

where $A(t)$, $B(t)$, and $C(t)$ are three time-dependent signals and $S_{AA}(\omega)$, $S_{BB}(\omega)$, and $S_{CC}(\omega)$ are their respective power spectral densities.

The above transformation is only valid when signals B and C are not correlated. We can see that by taking the autocorrelation of A :

$$\begin{aligned} \langle A(t)A(t+\tau) \rangle &= \langle B(t)B(t+\tau) \rangle + \underbrace{\langle B(t)C(t+\tau) \rangle + \langle C(t)B(t+\tau) \rangle}_{\text{cross-correlation terms}} \\ &\quad + \langle C(t)C(t+\tau) \rangle \end{aligned}$$

and noticing that only eliminating the cross-correlation terms gives:

$$\langle A(t)A(t+\tau) \rangle = \langle B(t)B(t+\tau) \rangle + \langle C(t)C(t+\tau) \rangle. \quad (1.7)$$

Applying the Fourier transform to both the sides of Eq. 1.7 and invoking the Wiener–Khinchin theorem gives:

$$S_{AA}(\omega) = S_{BB}(\omega) + S_{CC}(\omega). \quad (1.8)$$

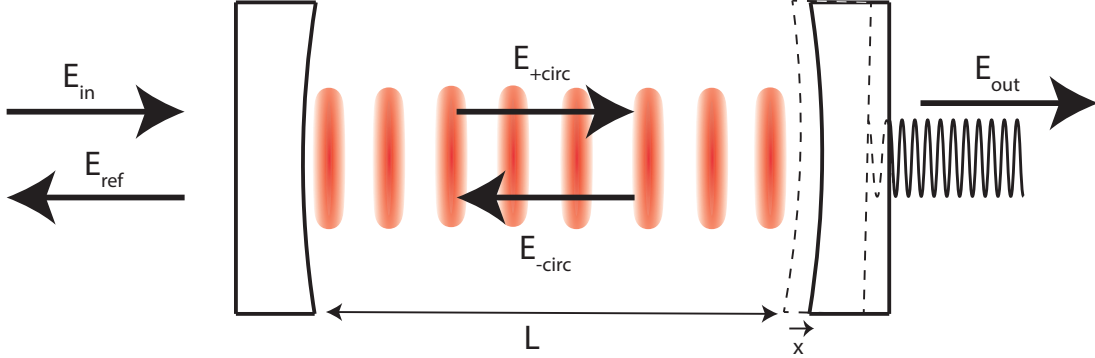


Figure 1.1: Schematic of a canonical 1-D optomechanical system, composed of an optical cavity (Fabry-Perot resonator) sandwiched between two mirrors, one of which is free to move.

1.2 Cavity optomechanical coupling

The canonical cavity optomechanical system consists of a Fabry-Perot cavity with a compliant end mirror (Fig. 1.1). We shall be interested in performing measurements of the displacement of the end-mirror by monitoring the phase or amplitude of the field leaking out of the cavity. Towards this end, we provide a basic description of the dynamics of the cavity optomechanical system, which are succinctly described by a pair of coupled differential equations [1, 6]:

$$m\ddot{x}(t) + m\gamma_m\dot{x}(t) + m\omega_m^2x(t) = F_{\text{ext}}(t) + F_{\text{RP}}(x, t) \quad (1.9a)$$

$$\dot{a}_c(t) = (\kappa + i(\omega_0 - \omega_c(x(t))))a_c(t) + \sqrt{2\kappa_1}E_{\text{in}}(t). \quad (1.9b)$$

Eq. 1.9a is the equation¹ of motion for a damped harmonic oscillator and describes the displacement, x , of the compliant end mirror. The variables m , γ_m , and ω_m are the effective mass, damping rate², and natural frequency of the mirror, respectively. $F_{\text{ext}}(t)$ is the sum of all the external forces on the mirror, excluding the radiation pressure force, $F_{\text{RP}}(t)$, which we shall return to shortly.

¹ We don't have to use vector notations for $x(t)$, $F(t)$, etc. as we are considering one-dimensional motion.

² Here, for simplicity, we are assuming a velocity-damped model.

Eq. 1.9b is the equation of motion for the *complex* amplitude, a_c , of the intracavity field in the slowly varying envelope approximation, normalized so that $|a_c(t)|^2$ is the energy of the intracavity field. The variables κ , ω_0 , ω_c , κ_1 , and E_{in} denote the energy decay rate of the cavity, the angular frequency of the input field, the resonance frequency of the cavity, the rate of energy decay through the input mirror, and the slowly varying complex amplitude of the input field, respectively.

The two equations are coupled via the position-dependent cavity resonance frequency:

$$\omega_c(x) = \frac{mc}{2(L+x)} \approx \omega_c(0) - Gx, \quad (1.10)$$

where m is the cavity mode order (an integer value), c is the speed of light, L is the nominal cavity length, and:

$$G \equiv -\frac{d\omega_c}{dx} \approx \frac{\omega_c}{L} \quad (1.11)$$

is the optomechanical coupling (a.k.a. frequency-pulling) factor.

To see how G enters into the dynamics of the mechanical resonator, note that for $x = 0$, the radiation force experienced by the mirror in Fig. can be written in several ways:

$$F_{\text{RP}}(t) = \frac{2P_{\text{circ}}(t)}{c} = \frac{|a_c(t)|^2}{L} = \frac{\hbar\omega_c n_c}{L} = \hbar G n_c = \frac{G|a_c(t)|^2}{\omega_c} \quad (1.12)$$

where $P_{\text{circ}}(t)$ is the power circulating in the optical cavity (the power incident on the end mirror) and n_c is the intracavity photon number [1].

Linearizing about small fluctuations, $a_c - \langle a_c \rangle$ and making the notational change: $a_c \rightarrow \langle a_c \rangle + a_c$, $F_{\text{RP}} \rightarrow \langle F_{\text{RP}} \rangle + F_{\text{RP}}$, etc., yields the linearized cavity optomechanical equations (assuming a stationary input field, $E_{\text{in}} = 0$):

$$m\ddot{x}(t) + m\gamma_m\dot{x}(t) + m\omega_m^2 x(t) = F_{\text{ext}}(t) + F_{\text{RP}}(x, t) \quad (1.13a)$$

$$\dot{a}_c(t) = (\kappa + i\Delta)a_c(t) + iGx(t)\langle a_c \rangle, \quad (1.13b)$$

where $\Delta = \langle \omega_0 \rangle - \langle \omega_c \rangle$ is the laser-cavity detuning, $\langle a_c \rangle = \sqrt{2\kappa_1} \langle E_{\text{in}} \rangle / (\kappa + i\Delta)$ is the mean cavity field, and $F_c(x, t) = G(\langle a_c \rangle a_c + \text{c.c.}) / \omega_c$ is the fluctuating radiation pressure force.

For the purposes of this thesis, we will assume that the cavity field responds instantaneously to the mechanical motion (the so-called “bad cavity limit”), in which case the LHS of Eq. 1.13b can be ignored, and the sensitivity of the intracavity field to mechanical motion becomes:

$$a_c(t) \approx \frac{iGx(t)}{\kappa + i\Delta} \langle a_c(t) \rangle. \quad (1.14)$$

Finally, the output field can be related to the circulating field by the input-output relation [1]:

$$E_{\text{out}}(t) = \sqrt{2k_2} a_c(t). \quad (1.15)$$

We note that, in the simplest case of a resonantly probed cavity ($\Delta = 0$), the phase of the output field, $\phi_{\text{out}}(t)$, can be expressed in terms of the position of the mechanical resonator in a familiar way:

$$\phi_{\text{out}}(t) \approx \frac{\text{Im}[E_{\text{out}}(t)]}{\text{Re}[E_{\text{out}}(t)]} = \frac{\text{Im}[a_c(t)]}{\text{Re}[a_c(t)]} = \frac{Gx(t)}{\kappa} = \frac{\omega_c x(t)}{L\kappa} = \frac{2\mathcal{F}x(t)}{\lambda}, \quad (1.16)$$

where $\mathcal{F} = \pi c / (L\kappa)$ is the cavity finesse.

More generally, taking the Fourier transform of both sides of Eq. 1.14, we can relate a_c and x by an optomechanical susceptibility:

$$\chi_{a_c x}(\omega) \equiv \frac{a_c(\omega)}{x(\omega)} = \frac{G}{\Delta + \omega - i\kappa}, \quad (1.17)$$

where, for completeness, we’ve retained the finite cavity response term, $\dot{a}_c(t)$, in Eq. 1.13b, leading to the term, ω , in the denominator (which is negligible in the bad cavity limit, $\omega \ll \kappa$).

1.3 Optomechanical measurement: Linear response model

In this thesis, we will adopt a semi-heuristic model for optomechanical measurement in which sensitivities will be characterized by linear

response functions and noise as an uncorrelated process with the appropriate power spectral density. The most important response will be the mechanical susceptibility, characterizing the displacement of a mechanical oscillator produced by external forces. The most important noises will be thermal noise (displacement noise intrinsic to the mechanical resonator) and shot noise (measurement noise intrinsic to the optical field).

In general, we describe the outcome of a measurement of the mechanical oscillator’s displacement as:

$$x_{\text{meas}}(t) = x(t) + x_{\text{imp}}(t), \quad (1.18)$$

where $x(t)$ is the physical motion of the oscillator and $x_{\text{imp}}(t)$ is the noise of the measurement tool—also known as imprecision noise—referred to as an apparent (and not physical) displacement.

We wish to infer from this measurement the magnitude of some environmental parameter that acts on the mechanical oscillator, producing displacement. Towards this end, we model the oscillator’s physical motion as produced by a total external force F_{tot} that contains several terms:

$$m\ddot{x}(t) + m\gamma_m\dot{x}(t) + m\omega_m^2x(t) = F_{\text{tot}}(t) \quad (1.19a)$$

$$= F_{\text{sig}}(t) + F_{\text{th}}(t) + F_{\text{ba}}(t); \quad (1.19b)$$

$F_{\text{sig}}(t)$ is the signal force whose properties we wish to determine; $F_{\text{th}}(t)$ is the thermal Langevin force (producing thermal motion, as we shall expand on later), and $F_{\text{ba}}(t) = F_{\text{RP}}(t)$ is a stochastic radiation pressure “back-action” force due to the optical readout field, also referred to as radiation pressure shot noise.

1.3.1 Measurement sensitivity in the frequency domain

Measurement sensitivity can be succinctly expressed in the frequency domain, in terms of power spectral densities. Towards this end, we apply the Fourier transform to both the sides of Eq. 1.18 and Eq. 1.19, yielding:

$$x_{\text{meas}}(\omega) = x(\omega) + x_{\text{imp}}(\omega). \quad (1.20)$$

and

$$x(\omega) = \chi_m(\omega)(F_{\text{sig}}(\omega) + F_{\text{th}}(\omega) + F_{\text{ba}}(\omega)), \quad (1.21)$$

where

$$\chi_m(\omega) = \frac{x(\omega)}{F(\omega)} = \frac{m^{-1}}{\omega^2 - \omega_m^2 + i\gamma_m\omega} \quad (1.22)$$

is the mechanical susceptibility.

Converting Eq. 1.20 and Eq. 1.21 to PSD units, we obtain:

$$S_{xx}^{\text{meas}}(\omega) = S_{xx}(\omega) + S_{xx}^{\text{imp}}(\omega) \quad (1.23a)$$

$$= |\chi_m(\omega)|^2(S_{FF}^{\text{sig}}(\omega) + S_{FF}^{\text{th}}(\omega) + S_{FF}^{\text{ba}}(\omega)) + S_{xx}^{\text{imp}}(\omega) \quad (1.23b)$$

$$\equiv |\chi_m(\omega)|^2(S_{FF}^{\text{sig}}(\omega) + S_{FF}^{\text{th}}(\omega) + S_{FF}^{\text{ba}}(\omega) + S_{FF}^{\text{imp}}(\omega)), \quad (1.23c)$$

where $S_{FF}^{\text{imp}}(\omega) = \chi_m^{-1}(\omega)S_{xx}^{\text{imp}}$ is the apparent force due to measurement imprecision noise.

In practice, the sum of measurement and thermal noise sets a lower bound on the signal, referred to as the measurement sensitivity:

$$S_{FF}^{\text{sig}}(\omega) \leq S_{FF}^{\text{th}}(\omega) + S_{FF}^{\text{ba}}(\omega) + S_{FF}^{\text{imp}}(\omega). \quad (1.24)$$

1.4 Sources of noise:

Here, we discuss the various kinds of noises that one encounters during a typical measurement in the lab. These noises can be either physical or apparent in nature. Physical noises correspond to actual fluctuations that are coupled to the motion of our mechanical resonator, while apparent noises are those fluctuations that *seem* to be arising from the resonator's motion; but in reality, do not carry any signatures of the oscillation. The resonator's thermal motion and the radiation pressure induced back-action force are examples of sources of "physical" noise, while the noise due to optical phase fluctuations contributes to only "apparent" motion.

1.4.1 Thermal noise:

A solid-state mechanical oscillator with a non-zero temperature is subject to thermal noise—random motion due, for example, to collisions with

thermally excited gas particles in the ambient environment. According to the fluctuation-dissipation theorem, the magnitude of the thermal motion is proportional to the (in general frequency-dependent) energy damping rate $\gamma_m(\omega)$, and can be expressed as a force spectral density [7]:

$$S_F^{\text{th}}(\omega) = \frac{4k_B T}{\omega} \text{Im}[\chi_m(\omega)^{-1}] = 4k_B T \gamma_m(\omega) m, \quad (1.25)$$

where T is the temperature of the environment (bath).

The thermal force drives the oscillator into thermal (“Brownian”) motion, characterized by a displacement noise spectrum:

$$S_x(\omega) = |\chi_m(\omega)|^2 S_F^{\text{th}}(\omega) = \frac{4k_B T \gamma_m(\omega)}{m} \frac{1}{(\omega_m^2 - \omega^2)^2 + \omega^2 (\gamma_m(\omega))^2}. \quad (1.26)$$

For velocity damping ($\gamma_m(\omega) = \gamma_m = \omega_m/Q_m$),

$$S_x(\omega)|_{\text{velocity damping}} = \frac{4k_B T \gamma_m(\omega_m)}{m} \frac{1}{(\omega_m^2 - \omega^2)^2 + \omega^2 \omega_m^2 / Q_m^2}; \quad (1.27)$$

while for “structural” damping (characteristic of the vibrational modes of elastic bodies), $\gamma_m(\omega) = \gamma_m(\omega_m) \times \omega_m/\omega = \omega_m^2/(\omega Q_m)$,

$$S_x(\omega)|_{\text{structural damping}} = \frac{4k_B T \gamma_m(\omega_m)}{m} \frac{\omega_m/\omega}{(\omega_m^2 - \omega^2)^2 + \omega_m^4 / Q_m^2}. \quad (1.28)$$

Note:

- Strictly speaking, Eq. (1.25) is only valid when the thermal phonon occupation of the oscillator $\bar{n}_{\text{th}} = (e^{(\hbar\omega_m)/(k_B T)} - 1)^{-1}$, is much greater than 1. When this doesn’t hold, the thermal energy term $k_B T$ in Eq. (1.25) can be replaced with the energy of a thermally excited quantum harmonic oscillator $\hbar\omega_m(\bar{n}_{\text{th}} + 1/2)$, yielding the the “Quantum” Fluctuation Dissipation Theorem:

$$S_F^{\text{th}}(\omega) = 4\hbar\omega_m(\bar{n}_{\text{th}} + \frac{1}{2})\gamma_m(\omega)m. \quad (1.29)$$

It’s interesting to note from the above equation, that when there are zero phonons (i.e. when $\bar{n}_{\text{th}} = 0$ at a temperature of 0 K), there is

still a "thermal" motion corresponding to $S_F^{\text{th}}(\omega) = 2\hbar\omega_m\gamma_m(\omega)m$ present—this is the zero-point motion. Experiments described later in this thesis were carried out at room temperature with sub-MHz oscillators ($\bar{n}_{\text{th}} \gtrsim 10^6$), and thus we will be using Eq. (1.25) only.

- There is also “extraneous” thermal noise from the components that make up the measurement apparatus, for example from the other optical mirror of a Fabry-Perot-type cavity optomechanical system (Fig. 1). In this thesis, we consider only the “intrinsic” thermal motion of the designated mechanical oscillator.

1.4.2 Photon shot noise (imprecision and backaction)

Heuristically, an optical field can be pictured as a current of randomly moving particles (“photons”) with well-defined energy $\hbar\omega_0$ and momentum $\hbar\omega_0/c$. The randomness of the photon flux manifests as a noise in the phase and amplitude of the optical field, giving rise to two forms of noise in an interferometric displacement measurement—imprecision noise (an apparent motion due to the random arrival of photons on the photodetector) and backaction noise (physical motion due to random arrival of momentum-transferring photons on the mechanical oscillator).

1.4.3 Imprecision shot noise

The first form of shot noise—imprecision shot noise—is an apparent motion due to the random arrival of photons on the photodetector, manifesting as a random phase fluctuation, $\delta\phi_{\text{shot}} \propto g\delta x_{\text{imp}}/\kappa$ (see Eq. 1.16). In the bad cavity limit ($\kappa \gg \omega_c$), the imprecision noise can be expressed as a displacement noise spectral density [1]:

$$S_{xx}^{\text{imp}}(\omega) = \frac{1}{32} \left(\frac{\kappa}{\bar{n}_c G^2} \right) \quad (1.30)$$

or equivalently:

$$S_{xx}^{\text{imp}}(\omega) = \frac{\pi\hbar c\lambda}{64} \left(\frac{1}{\eta\mathcal{F}^2 P} \right), \quad (1.31)$$

where $\eta \in [0, 1]$ is a unitless parameter characterizing the photodetector quantum efficiency [1].

1.4.4 Radiation pressure shot noise

The second form of shot noise—backaction shot noise—is the random physical motion produced by the momentum transfer of photons impinging on the mechanical oscillator. In the bad cavity limit, this “radiation pressure shot noise” can be expressed as an approximately frequency-independent force spectral density [1]:

$$S_{FF}^{\text{ba}}(\omega) = 8\hbar^2 \frac{\bar{n}_c G^2}{\kappa}. \quad (1.32)$$

The associated mechanical motion is given by:

$$S_{xx}^{\text{ba}}(\omega) \equiv |\chi_m(\omega)|^2 S_{FF}^{\text{ba}}. \quad (1.33)$$

Notably, from Eq. (1.30) and Eq. (1.32), we can see that:

$$S_{xx}^{\text{imp}}(\omega) S_{FF}^{\text{ba}}(\omega) \geq \frac{\hbar^2}{4}, \quad (1.34)$$

which is a signature of the Heisenberg Uncertainty Principle.

Chapter 2

DARK MATTER AND ITS DETECTION

Dark¹ matter is predicted to make up around eighty-five percent of the matter in our universe. Although dark matter cannot be explained by standard model physics, its existence is consistent with many astrophysical predictions; for example, it accounts for the extra mass required to hold galaxies together. Resolving the nature of DM is one of the biggest outstanding scientific problems and will help us understand the fundamental composition of our Universe. Some of the most popular candidates for DM are WIMPs (weakly interacting massive particles), axions, and sterile neutrinos. We, however, are concerned with the detection of ultralight dark matter (ULDM) using optomechanical force sensors.

2.1 Ultralight dark matter: phenomenology

It has been hypothesized that dark matter could be composed of non-thermally produced ultralight particles with mass $m_{\text{DM}} \lesssim 10 \text{ eV}/c^2$ [8]. For this mass range and the measured galactic halo DM density, these particles are inferred to be bosonic. If ULDM particles of mass $m_{\text{DM}} \lesssim 1 \text{ eV}/c^2$ are virialized with an average speed of $v_{\text{vir}} \sim 10^{-3}c$ [9], they would have a de Broglie wavelength of $\lambda_{\text{DM}} = h/(m_{\text{DM}}v_{\text{vir}}) \gtrsim 1 \text{ mm}$. Additionally, the local DM energy density of $\rho_{\text{DM}} \approx 0.4 \text{ GeV}/\text{cm}^3$ [10] would imply a large number of ULDM particles within a volume λ_{DM}^3 , implying, in turn, that they compose a coherent field, oscillating at a Compton frequency of $\omega_{\text{DM}} = m_{\text{DM}}c^2/\hbar \lesssim 2\pi \times 10^{14} \text{ Hz}$, with a Doppler-broadened linewidth of $\Delta\omega_{\text{DM}} = \omega_{\text{DM}}(\Delta v_{\text{vir}}/c)^2 \sim 10^{-6} \omega_{\text{DM}}$, where Δv_{vir} is the dispersion in the velocity of the ULDM particles. The ULDM field

¹ "Dark" matter is not dark-colored; rather it is invisible. It doesn't interact with baryonic matter and is thus invisible to electromagnetic radiation.

is analogous to an electromagnetic (EM) field and can be expressed as:

$$\phi(t, \mathbf{r}) \approx \phi_0 \cos(\omega_{\text{DM}}t - \mathbf{k}_{\text{DM}} \cdot \mathbf{r} + \theta_{\text{DM}}(t)), \quad (2.1)$$

where $\phi_0 \sim \sqrt{2\rho_{\text{DM}}}/\omega_{\text{DM}}^2$ and $k_{\text{DM}} = 2\pi/\lambda_{\text{DM}}$. The phase of the ULDM field, $\theta_{\text{DM}}(t)$, is considered to be roughly constant for coherence time $\tau_{\text{DM}} \equiv (2Q_{\text{DM}})/\omega_{\text{DM}} \approx 10^6/\omega_{\text{DM}}$, beyond which it diffuses to a value between 0 and 2π . This decoherence can be modeled by an exponentially decaying time auto-correlation [11]:

$$R(t_d) \equiv \langle \phi(t')\phi(t' + t_d) \rangle_{t'} \quad (2.2)$$

$$\approx \frac{\phi_0^2}{2} e^{-|t_d|/\tau_{\text{DM}}} \cos(\omega_{\text{DM}}t_d). \quad (2.3)$$

Invoking the Wiener-Khinchin theorem (Eq. 1.2a) thus yields a ULDM amplitude power spectral density of

$$S_{\phi\phi}^{\text{DM}}(\omega) = \int_{-\infty}^{\infty} dt_d e^{-i\omega t_d} R(t_d) \quad (2.4)$$

$$= \frac{\phi_0^2}{2} \left(\frac{\tau_{\text{DM}}}{1 + \tau_{\text{DM}}^2(\omega - \omega_{\text{DM}})^2} + \frac{\tau_{\text{DM}}}{1 + \tau_{\text{DM}}^2(\omega + \omega_{\text{DM}})^2} \right), \quad (2.5)$$

The above expression corresponds to a double-sided spectrum with two Lorentzian sidebands centered at $\omega = \pm \omega_{\text{DM}}$. We avoid dealing with negative frequencies by re-defining $S(\omega)$ as the total power spectral density detectable in a narrow-band filter, centered at $\omega \geq 0$:

$$S(\omega \geq 0) \equiv S(\omega) + S(-\omega). \quad (2.6)$$

We then get:

$$S_{\phi\phi}^{\text{DM}}(\omega \geq 0) = \phi_0^2 \left(\frac{\tau_{\text{DM}}}{1 + \tau_{\text{DM}}^2(\omega - \omega_{\text{DM}})^2} \right). \quad (2.7)$$

Therefore, the DM field's spectrum can be considered to be a Lorentzian with quality factor, $Q_{\text{DM}} \equiv \omega_{\text{DM}}/\text{FWHM} = (\omega_{\text{DM}}\tau_{\text{DM}})/2 \approx 5 \times 10^5$.

² In the next section, we will talk about a kind of ultralight DM known as "vector DM", where the amplitude, ϕ_0 , takes the form of a vector, $\boldsymbol{\phi}_0$, which characterizes the vector DM field, $\boldsymbol{\phi}(t, \mathbf{r})$.

We can express the DM field as a Lorentzian of linewidth (FWHM), γ_{DM} , whose power spectral density can be written as:

$$S_{\phi\phi}^{\text{DM}}(\omega) = \frac{S_{\phi\phi}^{\text{DM}}(\omega_{\text{DM}})}{1 + 4(\omega - \omega_{\text{DM}})^2/\gamma_{\text{DM}}^2}, \quad (2.8)$$

where $S_{\phi\phi}^{\text{DM}}(\omega_{\text{DM}})$ is the Lorentzian peak value [11]:

$$S_{\phi\phi}^{\text{DM}}(\omega_{\text{DM}}) \approx \frac{4 \langle \phi_0^2 \rangle}{\Delta\omega_{\text{DM}}} \approx \frac{2}{3} (a_0)^2 \frac{Q_{\text{DM}}}{\omega_{\text{DM}}}. \quad (2.9)$$

and the second equality assumes a randomly polarized DM field ($\langle \phi^2 \rangle \rightarrow \langle \phi^2 \rangle / 3$) [11].

2.2 Introducing the vector DM force and acceleration:

In this section, we will consider the force produced by ULDM particles based on the hypothesis that ULDM is a vector field composed of "dark photons" (DP). DP are vector (spin-1) bosons and we focus on a class of them that couples to the SM particles through direct gauge couplings.

The vector dark photon field can be represented as:

$$\boldsymbol{\phi}(t, \mathbf{r}) \approx \boldsymbol{\phi}_0 \cos(\omega t - \mathbf{k} \cdot \mathbf{r} + \theta_{\text{DM}}(t)), \quad (2.10)$$

where $|\boldsymbol{\phi}_0| \sim \sqrt{2\rho_{\text{DM}}}/\omega$ is the amplitude. The rest of the symbols are defined identically to those in Eq. (2.1).

Analogous to an EM-field, the dark photon field exerts a force on SM particles in proportional to their "DM charge" q [12, 11]

$$\mathbf{F}(t, \mathbf{r}) = q\boldsymbol{\phi}(t, \mathbf{r}). \quad (2.11)$$

For example, for a dark photon that couples to the baryon number, B , of a particle, we can write:

$$q = g_B B, \quad (2.12)$$

where g_B is the DM coupling strength to B . Similarly, for a dark photon field that couples to the baryon minus lepton number, $B - L$, of a particle, we can write:

$$q = g_{B-L}(B - L), \quad (2.13)$$

where g_{B-L} is the DM coupling strength to $B - L$.

In this thesis, we consider only $B - L$ coupling (for a discussion of the motivation, c.f. [12]). We can then express the dark photon force as:

$$\mathbf{F}(t, \mathbf{r}) = g_{B-L}(B - L)\mathbf{F}_0 \cos(\omega t - \mathbf{k} \cdot \mathbf{r} + \theta_{\text{DM}}(t)), \quad (2.14)$$

where:

$$|\mathbf{F}_0| \equiv \sqrt{2 \frac{e^2 \rho_{\text{DM}}}{\epsilon_0}} \approx 6 \times 10^{-16} \text{ N} \quad (2.15)$$

is found by equating the energy density of the gauge field to the DM energy density, ρ_{DM} [11], e refers to the electric charge of an electron, and ϵ_0 is the electric permittivity of free space.

For a neutral atom, $B - L$ is the neutron number. This means that $B - L$ dark photons can hypothetically be detected by mechanical systems made of neutrons (which is to say, most solid state mechanical systems). For example, the dark photon field would produce a differential acceleration of bodies with different neutron densities, or between bodies made of the same material which are separated by a distance comparable or larger than the de Broglie wavelength. Henceforth, we will consider only the time-variance of the DM force, since at frequencies of interest for optomechanical sensing (1 kHz - 1 MHz), the de Broglie wavelength is much larger than a typical laboratory.

Using Eq. 2.14 and noting $B - L = A - Z$ we can write the DM force on a single atom as [11]:

$$F_{\text{atom}}^{\text{DM}}(t) = g_{B-L}(A - Z)m_{\text{u}}a_0 \cos(\omega_{\text{DM}}t + \theta_{\text{DM}}(t)),$$

where $A(Z)$ is the mass (atomic) number, m_{u} is the atomic mass unit, and $a_0 = 3.7 \times 10^{11} \text{ m/s}^2$.

The force exerted by DM on a body of mass, m , made up of n atoms is:

$$F_m^{\text{DM}}(t) = n g_{B-L} (A - Z) m_u a_0 \cos(\omega_{\text{DM}} t + \theta_{\text{DM}}(t)). \quad (2.16)$$

Therefore, the acceleration of the body is given by:

$$a_m^{\text{DM}}(t) = \frac{F_m^{\text{DM}}(t)}{m} = \frac{F_m^{\text{DM}}(t)}{n A m_u} = g_{B-L} \frac{A - Z}{A} a_0 \cos(\omega_{\text{DM}} t + \theta_{\text{DM}}(t)). \quad (2.17)$$

The above equation implies that the DM produces an acceleration which depends only on the material of the body; as such, it's useful to think of the DM field as an *acceleration* field rather than a force field. We can express this field as

$$a_{\text{DM}}(t) = a_{\text{DM}} \cos(\omega_{\text{DM}} t + \theta_{\text{DM}}(t)), \quad (2.18)$$

where $a_{\text{DM}} = a_0 g_{B-L} (A - Z) / (\sqrt{3} A)$ and the factor of $\sqrt{3}$ accounts for polarization (see Eq. 2.9).

Finally, analogous to the PSD of the DM field expressed in Eq. 2.9, we can express the PSD of the DM acceleration field as a Lorentzian noise peak with a peak value of

$$S_{aa}^{\text{DM}}(\omega_{\text{DM}}) \approx \frac{4 \langle a_{\text{DM}}(t)^2 \rangle}{\Delta \omega_{\text{DM}}} \approx \frac{2}{3} \left(a_0 g_{B-L} \frac{A - Z}{A} \right)^2 \frac{Q_{\text{DM}}}{\omega_{\text{DM}}}. \quad (2.19)$$

2.3 A mechanical dimer for detecting dark matter:

In this section, we will describe the interaction between a $B - L$ ULDM field and a mechanical oscillator formed by two masses made of different materials, joined by a spring. We later use this “mechanical dimer” to model a generic inhomogeneous optomechanical sensor.

A sketch of the mechanical dimer is shown in Fig. 1a. The net force on mass 1 is given by

$$\begin{aligned} F_1(t) &= n_1 g_{B-L} (A_1 - Z_1) m_u a_0 \cos(\omega_{\text{DM}} t + \theta_{\text{DM}}) - kx(t) \\ &\equiv F_{m_1}^{\text{DM}}(t) - kx(t) \end{aligned}$$

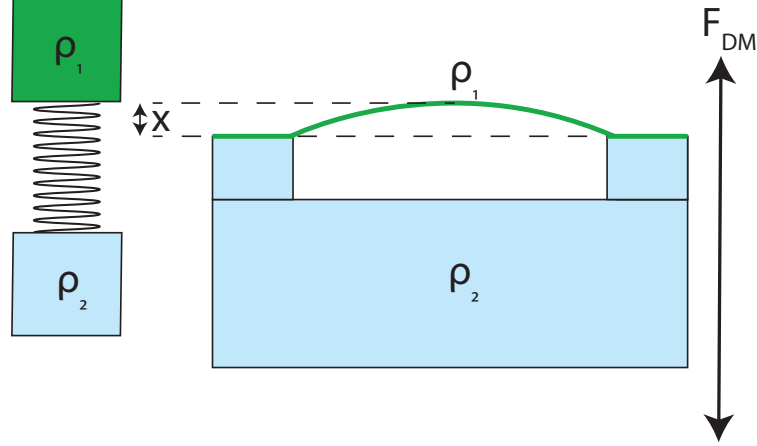


Figure 2.1: **Schematic of proposed mechanical-dimer DM sensor:** Left: lumped mass model. Right: membrane-based implementation. Variable ρ here refers to the density of the DM coupling charge (not to be mistaken with mass-density).

where n_1 is the total number of atoms that make up mass 1, k is the spring constant and $x(t) = x_1(t) - x_2(t)$ is the spring displacement.

Therefore, the acceleration of mass 1 is given by:

$$a_1(t) = \frac{F_1(t)}{m_1} = \frac{F_1(t)}{n_1 A_1 m_u} = g_{B-L} \frac{A_1 - Z_1}{A_1} a_0 \cos(\omega_{\text{DM}} t + \theta_{\text{DM}}) - \frac{kx(t)}{m_1}. \quad (2.20)$$

The net force on mass 2 is given by:

$$F_2(t) = n_2 g_{B-L} (A_2 - Z_2) m_u a_0 \cos(\omega_{\text{DM}} t + \theta_{\text{DM}}) + kx(t). \quad (2.21)$$

Thus, the acceleration of mass 2 is given by:

$$a_2(t) = \frac{F_2(t)}{m_2} = \frac{F_2(t)}{n_2 A_2 m_u} = g_{B-L} \frac{A_2 - Z_2}{A_2} a_0 \cos(\omega_{\text{DM}} t + \theta_{\text{DM}}) + \frac{kx(t)}{m_2}. \quad (2.22)$$

The relative acceleration of the 2 masses, $a_1(t) - a_2(t)$ is equal to the



Figure 2.2: Dimer model of the DM sensor

double-derivative of the spring's displacement, $\ddot{x}(t)$; i.e.

$$\ddot{x}(t) = a_1(t) - a_2(t) \quad (2.23)$$

$$= g_{B-L} \left(\frac{Z_2}{A_2} - \frac{Z_1}{A_1} \right) a_0 \cos(\omega_{\text{DM}} t + \theta_{\text{DM}}) - kx(t) \left(\frac{1}{m_2} + \frac{1}{m_1} \right). \quad (2.24)$$

We observe from Eq. 2.29, that, for a differential acceleration to exist between the two masses, they have to possess different atomic-mass number ratios (Z/A). Since the neutron-nucleon number ratio is equal to $1 - Z/A$, we can equivalently state that different neutron densities (i.e., different neutron-nucleon number ratios) lead to differential acceleration.

Eq. 2.24 can be re-expressed as the equation of motion for a harmonic oscillator:

$$\ddot{x}(t) + \omega_{\text{m}}^2 x(t) + a_{\text{rel}}^{\text{DM}}(t) = 0, \quad (2.25)$$

where $\omega_{\text{m}} = \sqrt{k/m_{\text{eff}}}$ is the resonance frequency, $m_{\text{eff}} = (m_1 m_2)/(m_1 + m_2)$ is the effective mass of the dimer, and $a_{\text{rel}}^{\text{DM}}(t)$ is the relative acceler-

ation of two *free* masses driven by the DM alone³:

$$a_{\text{rel}}^{\text{DM}}(t) = \frac{F_{m_2}^{\text{DM}}(t)}{m_2} - \frac{F_{m_1}^{\text{DM}}(t)}{m_1} \quad (2.26)$$

$$= g_{B-L} \left(\frac{Z_1}{A_1} - \frac{Z_2}{A_2} \right) a_0 \cos(\omega_{\text{DM}} t + \theta_{\text{DM}}) \quad (2.27)$$

$$= g_{B-L} f_{12} a_0 \cos(\omega_{\text{DM}} t + \theta_{\text{DM}}), \quad (2.28)$$

a f_{12} is the "suppression"⁴ factor" of the dimer:

$$f_{12} = \left| \frac{Z_1}{A_1} - \frac{Z_2}{A_2} \right|. \quad (2.29)$$

The magnitude of the relative acceleration between the dimer's masses is proportional to this suppression factor.

To introduce damping, we turn to the frequency domain, applying the Fourier transform to Eq. 2.25 and including an (in general frequency dependent) damping term, $i\omega\gamma_m(\omega)x(\omega)$, to get:

$$-\omega^2 x(\omega) + \omega_m^2 x(\omega) + i\omega\gamma_m(\omega)x(\omega) + a_{\text{rel}}^{\text{DM}}(\omega) = 0. \quad (2.30)$$

By rearranging the terms in the above equation, we get:

$$x(\omega) = (\omega^2 - \omega_m^2 - i\omega\gamma_m(\omega))^{-1} a_{\text{rel}}^{\text{DM}}(\omega) \quad (2.31a)$$

$$= \chi_{xa}(\omega) a_{\text{rel}}^{\text{DM}}(\omega), \quad (2.31b)$$

where:

$$\chi_{xa}(\omega) = x(\omega)/a_{\text{rel}}^{\text{DM}}(\omega) = (\omega^2 - \omega_m^2 - i\omega\gamma_m(\omega))^{-1} \quad (2.32)$$

is the acceleration susceptibility of our dimer-sensor.

We will now talk in terms of power spectral densities, which is what one deals with, typically, in a lab. Since $S_{xx}(\omega)/S_{aa}^{\text{DM}}(\omega) = |x(\omega)/a_{\text{rel}}^{\text{DM}}(\omega)|^2$

³ $a_{\text{rel}}^{\text{DM}}(t)$ is different from the net/physical relative acceleration between the two masses, $a_1(t) - a_2(t)$, which is given by Eq. 2.24.

⁴ Since Z/A is ≤ 1 , the $\Delta(Z/A) \equiv f_{12}$ is also ≤ 1 , and thus f_{12} is called a "suppression" factor as it reduces the relative acceleration between the two masses of the dimer.

and by considering structural damping $\gamma_m(\omega) = \omega_m^2/(\omega Q_m)$ (relevant for the internal modes of elastic bodies [7]), we can write:

$$S_{xx}^{\text{DM}}(\omega) = |\chi_{xa}(\omega)|^2 S_{aa}^{\text{DM}}(\omega) \quad (2.33a)$$

$$= ((\omega^2 - \omega_m^2)^2 + \omega_m^4/Q_m^2)^{-1} S_{aa}^{\text{DM}}(\omega). \quad (2.33b)$$

The above equation describes the sensitivity of the mechanical dimer to the DM signal to be measured, $S_{aa}^{\text{DM}}(\omega)$.

Finally, we replace the DM charge term from Eq. 2.19, $g_{B-L}(A-Z)/A$, with the dimer's effective DM charge, $g_{B-L}f_{12}$, to express the dimer's peak DM acceleration PSD as:

$$S_{aa}^{\text{DM}}(\omega_{\text{DM}}) \approx \frac{2}{3}(\beta g_{B-L}f_{12}a_0)^2 \frac{Q_{\text{DM}}}{\omega_{\text{DM}}}, \quad (2.34)$$

where β is a spatial overlap factor that accounts for more general mechanical mode shapes (e.g. $\beta = (4/\pi)^2$ for the fundamental mode of a membranes as in Fig. 1b [11], elaborated on below.

2.3.1 Some points to note on our dimer system's analysis:

- This model deals with only those masses that are of elemental form (made up of only one kind of atom). If there were different kinds of atoms (with different neutron-nucleon ratios) present in a mass, each kind would experience a different acceleration due to the different force from the DM field. Thus, the mass would experience different levels of internal stresses throughout its volume and would deform.

The force of the vector DM field on a molecule composed of n_i number of atoms is given by:

$$F_{\text{molecule}}^{\text{DM}}(t) = g_{B-L}m_u a_0 \cos(\omega_{\text{DM}}t + \theta_{\text{DM}}(t)) \sum_{i=1}^{n_1} (A_i - Z_i).$$

Thus, the total force of the vector DM field on mass 1 (m_1) is given by:

$$F_{m_1}^{\text{DM}}(t) = g_{B-L}m_u a_0 \cos(\omega_{\text{DM}}t + \theta_{\text{DM}}(t)) N_1 \sum_{i=1}^{n_1} (A_i - Z_i),$$

where N_1 is the total number of molecules that make up mass 1 (m_1).

$$\begin{aligned} a_{m_1}^{\text{DM}}(t) &= \frac{F_{m_1}^{\text{DM}}(t)}{m_1} = \frac{F_{m_1}^{\text{DM}}(t)}{N_1 m_u \sum_{i=1}^{n_1} A_i} \\ &= g_{B-L} a_0 \cos(\omega_{\text{DM}} t + \theta_{\text{DM}}(t)) \frac{\sum_{i=1}^{n_1} (A_i - Z_i)}{\sum_{i=1}^{n_1} A_i} \\ &= g_{B-L} a_0 \cos(\omega_{\text{DM}} t + \theta_{\text{DM}}(t)) \left(1 - \frac{\sum_{i=1}^{n_1} Z_i}{\sum_{i=1}^{n_1} A_i} \right). \end{aligned}$$

Similarly, for mass 2, we get:

$$a_{m_2}^{\text{DM}}(t) = g_{B-L} a_0 \cos(\omega_{\text{DM}} t + \theta_{\text{DM}}(t)) \left(1 - \frac{\sum_{i=1}^{n_2} Z_i}{\sum_{i=1}^{n_2} A_i} \right).$$

Therefore, the relative DM acceleration between the two masses is:

$$a_{m_1}^{\text{DM}} - a_{m_2}^{\text{DM}} = g_{B-L} a_0 \cos(\omega_{\text{DM}} t + \theta_{\text{DM}}(t)) \left(\frac{\sum_{i=1}^{n_2} Z_i}{\sum_{i=1}^{n_2} A_i} - \frac{\sum_{i=1}^{n_1} Z_i}{\sum_{i=1}^{n_1} A_i} \right)$$

We now define the suppression factor (f_{12}) to be equal to:

$$f_{12} = \left| \frac{\sum_{i=1}^{n_2} Z_i}{\sum_{i=1}^{n_2} A_i} - \frac{\sum_{i=1}^{n_1} Z_i}{\sum_{i=1}^{n_1} A_i} \right|.$$

Some suppression factors of dimers composed of the following pairs of materials (that are used widely in fabrication) are given:

- Silicon Nitride (Si_3N_4) and Silicon (Si):

$$f_{12} = \left| \frac{\sum_{i=1}^7 Z_i}{\sum_{i=1}^7 A_i} - \frac{Z_{\text{Si}}}{A_{\text{Si}}} \right| = \left| \frac{(14 \times 3) + (7 \times 4)}{(28 \times 3) + (14 \times 4)} - \frac{14}{28} \right| = 0 \quad (2.35)$$

- Si_3N_4 and Germanium (Ge):

$$f_{21} \approx 0.0676$$

- Si_3N_4 and Beryllium (Be):

$$f_{21} \approx 0.0556$$

Among the above three cases, the $\text{Si}_3\text{N}_4\text{-Ge}$ dimer would be the most sensitive relative-acceleration sensor, while the $\text{Si}_3\text{N}_4\text{-Si}$ dimer would not produce any differential acceleration.

- One might ask why we use a dimer and not a single-mass spring system? Let's say we did consider a single-mass spring system. The surface (ground, wall, Earth, etc.) which is attached to the spring is also some mass, under the action of a dark matter force. We should remember that the dark matter field is considered to be omnipresent and thus we cannot isolate any mass from its influence.
- Since the acceleration of a body due to gravity is independent of its mass, the gravitational accelerations would have cancelled out, had we included gravity in our analysis of the relative acceleration between the two masses. Even if we were considering a single spring-mass system suspended from the top of a ceiling under the action of gravity, all the equations would still hold good if we shift the equilibrium position accordingly to account for the gravitational force.
- In Eq. 2.20 and Eq. 2.22, we have considered $m = nAm_u$, which is actually an approximation as we have not accounted for binding energy (energy to assemble/disassemble a system of particles) in our calculations.

2.4 Measurement noise in dimer-based dark matter detector:

We now consider the noises entering the dimer-based dark matter detection scheme. Towards this end, we consider the equation of motion (excluding the damping term, which we will include in the Fourier domain) describing the dimer's oscillation:

$$\ddot{x}(t) + \omega_m^2 x(t) + a_{\text{rel}}^{\text{DM}}(t) + \underbrace{a_{\text{th}}(t) + a_{\text{ba}}(t)}_{\text{noise}} = 0, \quad (2.36)$$

where $a_{\text{th}}(t)$ and $a_{\text{ba}}(t)$ are the thermal and back-action acceleration noises, respectively.

The measurement of the dimer's motion can be expressed as a sum of the physical motion x and imprecision noise x_{imp} :

$$x_{\text{meas}}(t) = x(t) + x_{\text{imp}}(t) \quad (2.37a)$$

$$= x_{\text{DM}}(t) + x_{\text{th}}(t) + x_{\text{ba}}(t) + x_{\text{imp}}(t). \quad (2.37b)$$

Taking the Fourier transform of Eq. 2.37b and including structural damping as in Eq. 2.30 yields

$$x_{\text{meas}}(\omega) = x(\omega) + x_{\text{imp}}(\omega) \quad (2.38a)$$

$$= \chi_{xa}(\omega) (a_{\text{rel}}^{\text{DM}}(\omega) + a_{\text{th}}(\omega) + a_{\text{ba}}(\omega)) + x_{\text{imp}}(\omega) \quad (2.38b)$$

where $\chi_{xa}(\omega) = (\omega^2 - \omega_m^2 + i\omega_m^2/Q)$ is the acceleration susceptibility as defined in Eq. 2.32.

Converting to power spectral densities, we get:

$$S_{xx}^{\text{meas}}(\omega) = S_{xx}^{\text{DM}}(\omega) + S_{xx}^{\text{th}}(\omega) + S_{xx}^{\text{ba}}(\omega) + S_{xx}^{\text{imp}}(\omega) \quad (2.39a)$$

$$= |\chi_{xa}(\omega)|^2 (S_{aa}^{\text{DM}}(\omega) + S_{aa}^{\text{th}}(\omega) + S_{aa}^{\text{ba}}(\omega)) + S_{xx}^{\text{imp}}(\omega). \quad (2.39b)$$

From Eq. 1.25, we can write the thermal acceleration noise as:

$$S_{aa}^{\text{th}}(\omega) = \frac{S_{FF}^{\text{th}}(\omega)}{m_{\text{eff}}^2} = \frac{2k_B T_m \gamma_m(\omega)}{m_{\text{eff}}} = \frac{2k_B T_m \omega_m}{m_{\text{eff}} Q_m} \frac{\omega_m}{\omega}, \quad (2.40)$$

where $m_{\text{eff}} = \frac{m_1 m_2}{m_1 + m_2}$ is the effective mass of the dimer (see Eq. 2.25).

For the imprecision noise S_{xx}^{imp} and backaction noise S_{xx}^{ba} , we envision the two masses comprising the dimer as end-mirrors of a Fabry-Perot cavity, forming a cavity optomechanical system. Thus following Eq. 1.31 and 1.4.4 we identify $S_{xx}^{\text{imp}}(\omega) = \frac{\pi \hbar c \lambda}{64 \mathcal{F}^2 P}$ and $S_{aa}^{\text{ba}}(\omega) = \frac{\hbar^2}{m_{\text{eff}}^2 S_{xx}^{\text{imp}}(\omega)}$, respectively.

Rearranging once again, we identify minimum DM signal that can be detected, with the total measurement noise (see Sec. 1.4):

$$S_{aa}^{\text{meas}}(\omega) = S_{aa}^{\text{th}}(\omega) + S_{aa}^{\text{ba}}(\omega) + |\chi_{xa}(\omega)|^{-2} S_{xx}^{\text{imp}}(\omega). \quad (2.41)$$

Recalling Eq. 2.34 for the resonance DM signal

$$S_{aa}^{\text{DM}}(\omega_{\text{DM}}) \approx \frac{2}{3} (\beta g_{B-L} f_{12} a_0)^2 \frac{Q_{\text{DM}}}{\omega_{\text{DM}}}.$$

and equating with the resonant measurement noise, $S_{aa}^{\text{meas}}(\omega_{\text{DM}})$, we reason that the coupling parameter g_{B-L} can be bound from below as

$$g_{B-L} \geq \frac{\sqrt{3/2}}{\beta f_{12} a_0} \sqrt{S_{aa}^{\text{meas}}(\omega_{\text{DM}}) \frac{\omega_{\text{DM}}}{Q_{\text{DM}}}}. \quad (2.42)$$

If we further assume that the resonance frequency of the mechanical device matches the DM frequency ($\omega_m = \omega_{\text{DM}}$), and that our measurement is dominated by thermal noise ($S_{aa}^{\text{meas}}(\omega_{\text{DM}}) \approx S_{aa}^{\text{th}}(\omega_{\text{DM}})$), we predict a lower bound of [11]

$$g_{B-L}^{\text{th}} \geq \frac{\sqrt{3/2}}{\beta f_{12} a_0} \sqrt{\frac{4k_B T \omega_{\text{DM}}^2}{m_{\text{eff}} Q_m Q_{\text{DM}}}}. \quad (2.43)$$

2.5 Improving resolution by time averaging

In this section, following [11], we will consider how time-averaging can improve the resolution of the DM search. We first note that in practice all measurements are of finite duration, and therefore the PSD of a stochastic process can be only estimated. This estimate, called a periodogram, is computed by taking the Discrete Fourier Transform of the measurement record. Averaging several independent periodograms—“Bartlett’s method”—gives a successively better estimate of the PSD.

Specifically, consider a finite-duration record of stochastic signal $a(t)$ characterized by finite-time Fourier transform $a_T(\omega) = \int_{t_0}^{t_0+T/2} a(t) e^{i\omega t} dt$. The periodogram is given by $\mathcal{P}_{aa}^T(\omega) \equiv |a_T(\omega)|^2 / \Delta f$, where $\Delta f = 1/T$ is the resolution bandwidth. We define $\mathcal{P}_{aa}^{T,N}(\omega) \equiv \langle \mathcal{P}_{aa}^T(2\pi f) \rangle_N$ as the average of N independent periodograms (e.g., by choosing t_0 so that the measurement intervals don’t overlap). According to Bartlett’s method, $\mathcal{P}_{aa}^{T,N}(\omega)$ converges to the smoothed (over bandwidth Δf) PSD given by Wiener-Khinchin theorem (Eq. 1.2a) in the limit $N \rightarrow \infty$, i.e.

$$\mathcal{P}_{aa}^{T,N}(2\pi f) \equiv \frac{\langle |a_T(\omega)|^2 \rangle_N}{\Delta f} \xrightarrow{N \rightarrow \infty} \frac{1}{\Delta f} \int_{f-\Delta f/2}^{f+\Delta f/2} S_{aa}(2\pi f') df' \quad (2.44)$$

The standard deviation of the PSD estimate $\Delta\mathcal{P}_{aa}^{T,N}(\omega)$ plays an important role in parameter estimation, as it sets the PSD of the smallest signal $a_{\text{sig}}(t)$ that can be distinguished from $a(t)$ in a measurement of the form $a(t) + a_{\text{sig}}(t)$. For a Gaussian noise process $a(t)$, $\Delta\mathcal{P}_{aa}^{T,N}(\omega) \approx S_{aa}(\omega)/\sqrt{N}$ [13] which implies that smaller a_{sig} can be measured with longer total measurement times $\tau \equiv NT$. The scaling with τ however depends on whether $a_{\text{sig}}(t)$ is coherent or incoherent over τ . We consider these two cases below, for the case of our partially coherent DM signal $a_{\text{DM}}(t)$ (Eq. 2.18) with coherence time τ_{DM} [11]:

- Total measurement time $\tau < \tau_{\text{DM}}$:

For total measurement time $\tau = NT < \tau_{\text{DM}}$, the signal is coherent and the optimal strategy to make a signal measurement $\tau = T$. The total power in periodogram at $\omega = \omega_m$ is $\mathcal{P}_{aa}^T(\omega_m)\Delta f + \langle a_{\text{DM}}^2 \rangle$ and the standard deviation is $\Delta\mathcal{P}_{aa}^T(\omega_m)\Delta f \approx S_{aa}(\omega_m)/\tau$. The minimum coupling parameter $g_{\text{B-L}}$ that can be resolved thus scales as

$$g_{\text{B-L}}^{\min} \propto \sqrt{\frac{S_{aa}(\omega_m)}{\tau}}. \quad (2.45)$$

where a is the total measurement noise.

- For total measurement time $\tau > \tau_{\text{DM}}$:

For total measurement time $\tau = NT > \tau_{\text{DM}}$, the measurement record can be divided into approximately $N = \tau/\tau_{\text{DM}}$ statistically independent measurements, and periodograms can be averaged using Bartlett's method. The total power in the averaged periodogram at $\omega = \omega_m$ is $(\mathcal{P}_{aa}^{T,N}(\omega_m) + \mathcal{P}_{a_{\text{DM}}a_{\text{DM}}}^{T,N}(\omega_m))\Delta f$, which for sufficiently large N is approximately $(S_{aa}(\omega_m) + S_{aa}^{\text{DM}}(\omega_m))\Delta f$. Assuming the measurement is dominated by noise, the standard deviation of the power estimate is $\Delta\mathcal{P}_{aa}^{T,N}(\omega_m)\Delta f \approx S_{aa}(\omega_m)/\sqrt{N}$. The minimum coupling parameter $g_{\text{B-L}}$ that can be resolved thus scales as

$$g_{B-L}^{\min} \propto \sqrt{\frac{S_{aa}(\omega_{\text{DM}})}{\tau_{\text{DM}}}} \left(\frac{\tau_{\text{DM}}}{\tau}\right)^{1/4}. \quad (2.46)$$

where again $a(t)$ represents the measurement noise.

Combining Eq. 2.45 and Eq. 2.46 with Eq. 2.42 we get

$$g_{B-L}(\omega) \geq \frac{\sqrt{3}}{\beta f_{12} a_0} \sqrt{\frac{S_{aa}^{\text{meas}}(\omega)}{\tau_{\text{DM}}}} \times \begin{cases} (\frac{\tau_{\text{DM}}}{\tau})^{1/2}, & \tau \lesssim \tau_{\text{DM}} \\ (\frac{\tau_{\text{DM}}}{\tau})^{1/4}, & \tau \gg \tau_{\text{DM}}. \end{cases} \quad (2.47)$$

and the thermal limit (see Eq. 2.43):

$$g_{B-L}^{\text{th}} \geq \frac{\sqrt{3/2}}{\beta f_{12} a_0} \sqrt{\frac{4k_B T \omega_{\text{DM}}^2}{\mu Q_m Q_{\text{DM}}}} \times \begin{cases} (\frac{\tau_{\text{DM}}}{\tau})^{1/2}, & \tau \lesssim \tau_{\text{DM}} \\ (\frac{\tau_{\text{DM}}}{\tau})^{1/4}, & \tau \gg \tau_{\text{DM}}, \end{cases} \quad (2.48)$$

where $\tau_{\text{DM}} = 2Q_{\text{DM}}/\omega_{\text{DM}}$ is the DM coherence time and τ is the total measurement time.

2.6 Experimental apparatus for DM detection:

The proposed experimental apparatus for DM detection consists of a dual Si_3N_4 membrane cavity-optomechanical accelerometer attached to a Germanium reference plate, as shown in Fig. 2.3. We are currently

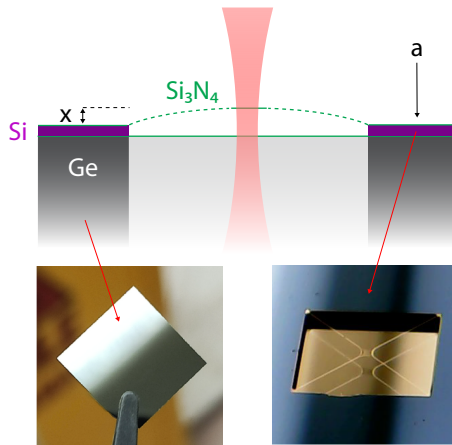


Figure 2.3: Schematic of proposed membrane-based DM detector

focusing on the dual membrane accelerometer and provide an outline of its properties in the following section.

2.6.1 Trampoline-on-membrane (TOM) accelerometer

We fabricated the device shown in Fig. 2.4, consisting of a $2.5 \text{ mm} \times 2.5 \text{ mm} \times 7.5 \text{ nm}$ silicon nitride (Si_3N_4) "trampoline" suspended opposite a square membrane of similar dimensions on a 0.2 mm thick silicon (Si) chip. The trampoline serves as a test mass for acceleration of the chip, to which the relatively stiffer square membrane is rigidly attached. The trampoline has a $200 \mu\text{m}$ - wide pad and $200 \mu\text{m}$ - wide tethers, with fillets tailored to optimize the Q of the fundamental trampoline mode. For these dimensions, the fundamental resonance frequency of the trampoline is $\omega_1 = 2\pi \cdot 40 \text{ kHz}$, and the physical mass and Q of the trampoline are $m_1 = 12 \text{ ng}$ and $Q_1 = 1.1 \times 10^7$, respectively, implying a thermal acceleration sensitivity of $S_a^{\text{th}} = 0.56 \mu\text{g}/\sqrt{\text{Hz}}$.

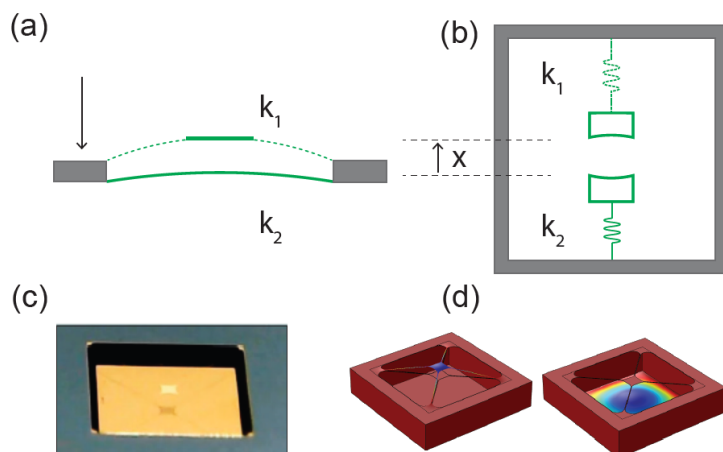


Figure 2.4: **Trampoline-on-membrane accelerometer** (taken with permission from [14]): (a) Schematic of the device: a pair of membranes with different stiffnesses, attached to a common base respond differently to base acceleration. (b) Each membrane can be considered to be a spring-mass system suspended from a common frame. The membranes form a Fabry-Perot end-mirrors. (c) Photo of the fabricated device. (d) Finite-element simulation of the fundamental flexural modes of the device.

Details about the characterization of the TOM accelerometer are discussed in Fig. 2.5 and a set of room temperature temperature acceleration measurements, limited by both thermal noise and imprecision noise, are described in Fig. 2.6. The noise floor of the accelerometer, shown in the bottom of Fig. 2.6, is used to obtain the (hypothetical) DM and (actual) CSL constraints in Fig. 4.1 and Fig. 4.2, respectively.

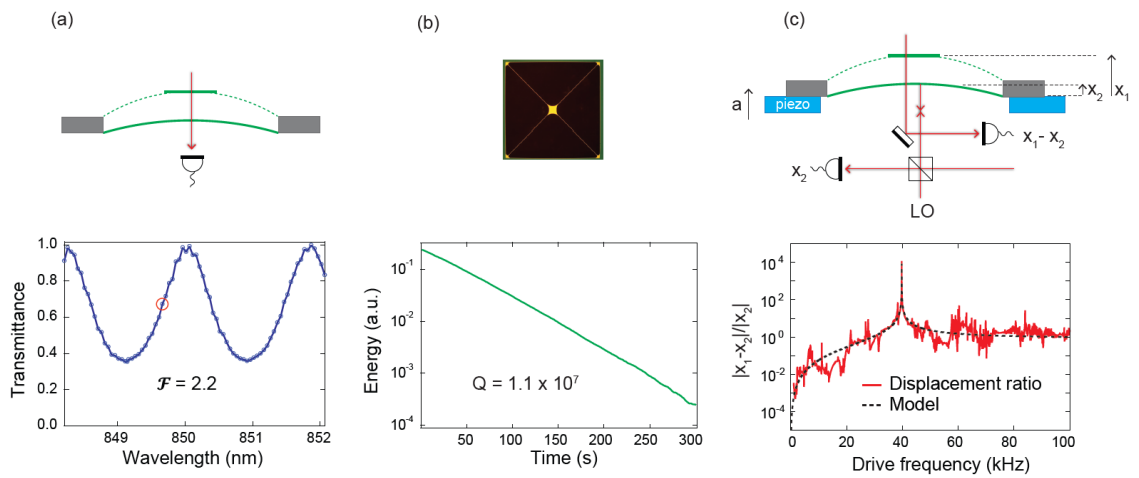


Figure 2.5: **Characterization of TOM accelerometer** (taken with permission from [14]): (a) Optical transmission versus wavelength near 850 nm. A finesse of 2.2 is obtained by fitting the interference fringes to an Airy function. Readout is carried out near the fringe midpoint, highlighted by a red circle. (b) Optical micrograph (above) of the trampoline membrane and energy ringdown (below) of its fundamental flexural mode. Fitting to an exponential yields a $Q = 1.1 \times 10^7$. (c) Above: Scheme for characterizing the response of the dual-membrane accelerometer (top) to a base excitation. Below: measurement of the response at frequencies below the fundamental resonance of the rigid membrane (120 kHz). Near the 40 kHz trampoline resonance, the response is approximated by the mechanical susceptibility of the trampoline alone.

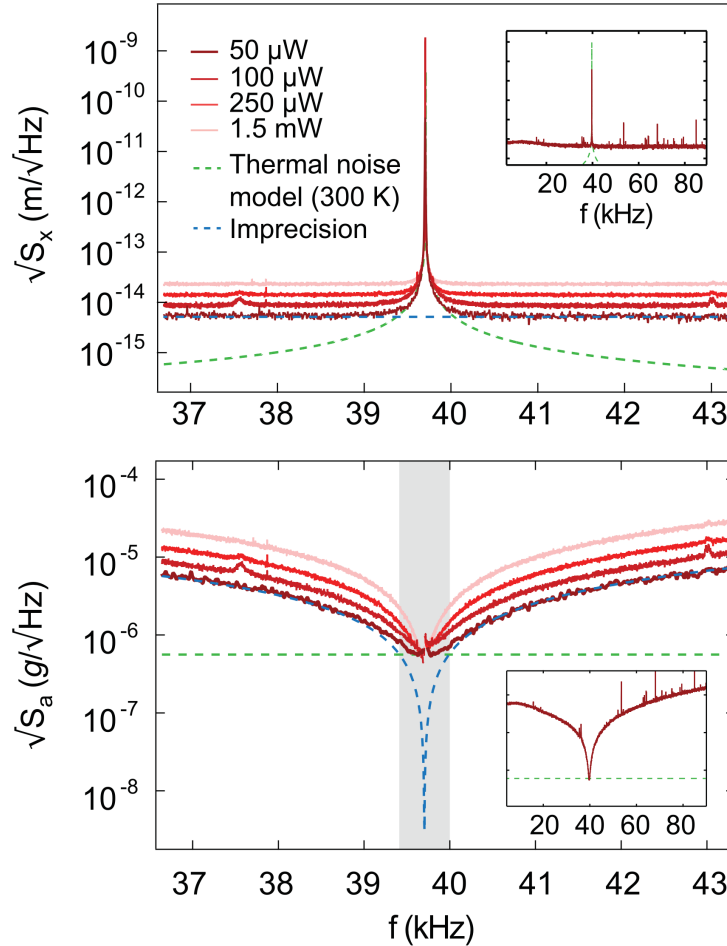


Figure 2.6: **Sensitivity of TOM accelerometer** (taken with permission from [14]): Acceleration noise floor (bottom) inferred by dividing the displacement spectrum (top) by the acceleration susceptibility. Darker shades of red correspond to larger optical powers. Gray shading indicates the resonant bandwidth over which thermal noise dominates imprecision noise for the largest output power, $P_{\text{out}} = 1.5$ mW.

Chapter 3

COLLAPSE MODELS AND THEIR DETECTION

3.1 Spontaneous wave function collapse models:

The Schrödinger equation describes deterministic evolution of the wave function as a linear superposition of different states, but a measurement of a system always yields a single state. This conflict is what is referred to as the “measurement problem” in quantum mechanics. Spontaneous wave function collapse models [15] seek to resolve the measurement problem by stating that the Schrodinger evolution is an approximation; one which turns out to be good for microscopic systems, but fails as the size/complexity of the system increases. Thus, spontaneous wave function collapse models, also called objective-collapse theories or dynamical reduction models [16], probe the gap between our understanding of the classical and quantum world.

In collapse theories, the Schrödinger equation is supplemented with additional nonlinear and stochastic terms which localize the wave function in space. The resulting dynamics is such that for microscopic, isolated systems, the new terms have a negligible effect; therefore, the usual quantum properties are recovered, apart from tiny deviations. By contrast, an inbuilt amplification mechanism makes sure that for macroscopic systems consisting of many particles, the collapse becomes stronger than the quantum dynamics. Then their wave function is always well-localized in space, so well-localized that it behaves, for all practical purposes, like a point moving in space according to Newton’s laws. In this sense, collapse models provide a unified description of microscopic and macroscopic systems, avoiding the conceptual problems associated with measurements in quantum theory.

Commonly studied collapse models are:

- Continuous spontaneous localization (CSL) model [17]

- Ghirardi–Rimini–Weber (GRW) model [18]
- Diósi–Penrose (DP) model [19]

These models stand in opposition to many-worlds interpretation theories, in that they hold that a process of wave function collapse curtails the branching of the wave function and removes unobserved behavior.

The fundamental dynamics of collapse models is given by the following stochastic differential equation for the wave function [15, 19]:

$$d|\psi_t\rangle = \left[\frac{-i}{\hbar} \mathbf{H} dt + \sqrt{\lambda} (\mathbf{A} - \langle \mathbf{A} \rangle_t) dW_t - \frac{\lambda}{2} (\mathbf{A} - \langle \mathbf{A} \rangle_t)^2 dt \right] |\psi_t\rangle, \quad (3.1)$$

where \mathbf{H} is the Hamiltonian of the system and $\langle \mathbf{A} \rangle_t = \langle \psi_t | \mathbf{A} | \psi_t \rangle$ is the expectation value of some operator, \mathbf{A} , assumed to be self-adjoint. \mathbf{A} , for example, could be the position or the 1-D spin operator. λ is a positive constant, which sets the strength of the collapse mechanism and W_t is a standard Wiener process.

Eq. 3.1 describes a diffusion process on the unit sphere of a Hilbert space. \mathbf{H} induces a unitary "rotation" on the sphere, while the remaining terms tend to *collapse* the wave function towards one of the eigenstates of the operator, \mathbf{A} , in a stochastic fashion. If the dynamics induced by \mathbf{H} is dominant, then the evolution is deterministic and only slightly "blurred" by the collapse terms, for very long times. Alternatively, if the collapse terms are dominant, then the wave function collapses very rapidly in a random fashion, with the probabilities that seem to be consistent with the Born rule.

3.2 The continuous spontaneous localization (CSL) model

Our study deals with the continuous spontaneous localization (CSL) model, which is the most widely studied type of collapse model. The CSL model was proposed by Philip Pearle in 1989 [20] and finalized by Pearle, Gian Carlo Ghirardi, and Alberto Rimini in 1990 [17]. It describes the wave function to be continuously collapsing in time while choosing the convenient basis of position to describe localization. Negligible effects of

this model are predicted for microscopic systems; while they become evident in macroscopic systems, as ensured by the amplification mechanism. It is to be noted that the symmetry of identical particles is maintained.

The experiments testing the CSL model can be divided into interferometric and non-interferometric experiments, which probe direct and indirect effects of the collapse mechanism, respectively:

- Interferometric experiments try to detect the direct action of the collapse, namely, the spatial localization of the wavefunction. They include the experiments where a superposition is created, followed by a probe in its interference pattern. CSL reduces the interference contrast, which is expressed mathematically by the reduction of the off-diagonal terms of the statistical operator [21].
- Non-interferometric experiments consist of CSL tests that are not based on the preparation of a superposition. They exploit an indirect effect of the collapse, which consists of a Brownian motion induced by the interaction with the collapse noise. The effect of this noise amounts to an effective stochastic force acting on the system, and several kinds of experiments can be designed to quantify such a force, like those probing:
 - Radiation emission from charged particles [22]
 - Heating in bulk materials [23]
 - Diffusive effects ¹ [24, 25]

The CSL model is characterized [26] by two phenomenological parameters, the collapse rate, λ , and the correlation length of the noise, r_c . λ sets the frequency of the collapse, while r_c can be used to quantify the strength of the collapse. That is, superpositions of lengths greater than r_c correspond to strong collapses; while superposition of sizes lower than r_c would imply a weaker collapse.

¹We seek to explore this particular signature of CSL, which we will detail upon in the next section.

3.3 CSL-induced forces and torques:

In this section, we ² will derive the forces and torques that are hypothesized by CSL theory, to act on mechanical bodies, like on our nanomembrane and torsion paddle. Our derivation of the CSL momentum diffusion rate (Eq. 3.9) follows similar derivations in [27, 25, 28, 24, 29, 30, 31].

3.3.1 CSL momentum diffusion:

The dynamics of a *rigid* body subject to continuous spontaneous localization (CSL) is described by the master equation [31]:

$$\dot{\rho} = (\mathcal{L} + \mathcal{L}_{\text{CSL}})\rho, \quad (3.2)$$

where \mathcal{L} is the Liouvillian operator associated with standard quantum mechanics:

$$\mathcal{L}\rho = -\frac{i}{\hbar}[H, \rho] \quad (3.3)$$

and \mathcal{L}_{CSL} is a correction due to CSL:

$$\mathcal{L}_{\text{CSL}}\rho = -\frac{\lambda_{\text{CSL}}}{2r_{\text{CSL}}^3 \pi^{3/2} m_0^2} \int [M(\mathbf{r}), [M(\mathbf{r}), \rho]] d^3\mathbf{r}, \quad (3.4)$$

where:

$$M(\mathbf{r}) = \sum_n m_n e^{(\mathbf{r}-\mathbf{r}_n)^2/2r_{\text{CSL}}^2} \quad (3.5)$$

is the mass operator that describes the localization of constituent atoms of masses, m_n , position, \mathbf{r}_n , within a radius, r_{CSL} , and at a rate, λ_{CSL} .

CSL leads to diffusion of the linear and angular momenta of the body. To decouple these degrees of freedom, we consider rotation about one of the principal axes of the body. The master equation can then be written:

$$\mathcal{L}_{\text{CSL}}\rho = -\frac{1}{\hbar^2} \left(D_{\text{CSL}}^{(x)} [x, [x, \rho]] + D_{\text{CSL}}^{(\phi)} [\phi, [\phi, \rho]] \right), \quad (3.6)$$

where $D_{\text{CSL}}^{(x)}$ is the linear momentum diffusion rate and $D_{\text{CSL}}^{(\phi)}$ is the angular momentum diffusion rate.

²This section was primarily the work of our advisor, Dr. Dalziel Wilson. Many thanks to him!

Phenomenologically, the linear momentum diffusion can be viewed as a stochastic force, $F_{\text{CSL}}(t)$, with autocorrelation, $\langle F_{\text{CSL}}(t)F_{\text{CSL}}(t') \rangle = D_{\text{CSL}}\delta(t - t')$, and single-sided PSD:

$$S_F^{\text{CSL}}(\omega) = 2D_{\text{CSL}}^{(x)}. \quad (3.7)$$

Likewise, angular momentum diffusion can be viewed as a stochastic torque, $\tau_{\text{CSL}}(t)$, with PSD:

$$S_\tau^{\text{CSL}}(\omega) = 2D_{\text{CSL}}^{(\phi)}. \quad (3.8)$$

For center-of-mass motion in the x -direction, the linear momentum diffusion rate can be expressed as:

$$D_{\text{CSL}}^{(x)} = \lambda_{\text{CSL}} \frac{\hbar^2 r_{\text{CSL}}^3}{\pi^{3/2} m_0^2} \int e^{-r_{\text{CSL}}^2 k^2} k_x^2 |\tilde{\rho}_m(\mathbf{k})|^2 d^3 k, \quad (3.9)$$

where $\tilde{\rho}_m(\mathbf{k}) = \int \rho_m(\mathbf{r}) e^{-i\mathbf{k}\cdot\mathbf{r}} d^3 \mathbf{r}$ is the Fourier transform of the mass density, $\rho_m(\mathbf{r})$, which is also called as the ‘‘structural factor’’.

Similarly, for rotation about a principal axis as the z -axis, the angular momentum diffusion rate can be expressed as ³:

$$D_{\text{CSL}}^{(\phi)} = \lambda_{\text{CSL}} \frac{\hbar^2 r_{\text{CSL}}^3}{\pi^{3/2} m_0^2} \int e^{-r_{\text{CSL}}^2 k^2} |(k_y \partial_{k_x} - k_x \partial_{k_y}) \tilde{\rho}_m(\mathbf{k})|^2 d^3 k. \quad (3.10)$$

Equations 3.9 and 3.10 can be greatly simplified for homogeneous bodies ($\rho_m(\mathbf{r}) = \rho_0$), whose dimensions are much larger than the characteristic length, r_{CSL} .

3.3.2 CSL-induced force on a nanomembrane:

We consider a very thin plate (thickness $\sim r_{\text{CSL}}$) embodied by a Si_3N_4 nanomembrane; e.g. the central pad of the trampoline in our TOM device. To ensure that the membrane acts like a rigid body, we consider a trampoline whose tethers are much less massive than the central pad.

³ Here, ∂_{k_x} and ∂_{k_y} are short-hands for $\frac{\partial}{\partial k_x}$ and $\frac{\partial}{\partial k_y}$, respectively.

We consider a rectangular plate with dimensions, $b_X \times b_Y \times b_Z$, along its axes, X , Y and Z . Its structure factor is thus:

$$\tilde{\rho}_m(\mathbf{k}) = m \operatorname{sinc}\left(\frac{k_X b_X}{2}\right) \operatorname{sinc}\left(\frac{k_Y b_Y}{2}\right) \operatorname{sinc}\left(\frac{k_Z b_Z}{2}\right), \quad (3.11)$$

where $m = \rho_0 b_X b_Y b_Z$ is the total mass of the plate. If we assume the axes of the membrane to superimpose with the corresponding cartesian coordinate axes, we get $x = X$, $y = Y$, and $z = Z$.

The effective CSL force acting on the membrane is:

$$S_F^{\text{CSL}}(\omega) = 2\lambda_{\text{CSL}} \frac{\hbar^2 r_{\text{CSL}}^3 m^2}{\pi^{3/2} m_0^2} \int k_x^2 e^{-k_x^2 r_{\text{CSL}}^2} \operatorname{sinc}^2\left(\frac{k_x b_x}{2}\right) dk_x \quad (3.12a)$$

$$\times \int e^{-k_y^2 r_{\text{CSL}}^2} \operatorname{sinc}^2\left(\frac{k_y b_y}{2}\right) dk_y \int e^{-k_z^2 r_{\text{CSL}}^2} \operatorname{sinc}^2\left(\frac{k_z b_z}{2}\right) dk_z \quad (3.12b)$$

$$\approx \lambda_{\text{CSL}} \frac{\hbar^2 r_{\text{CSL}}^2 m^2}{m_0^2} \frac{16\pi}{b_x^2 b_y b_z r_{\text{CSL}}} (1 - e^{-b_x^2/2r_{\text{CSL}}^2}) \quad (3.12c)$$

$$\approx \lambda_{\text{CSL}} \frac{16\pi \hbar^2 r_{\text{CSL}}^2}{m_0^2} \frac{\rho_0 m}{b_x} (1 - e^{-b_x^2/2r_{\text{CSL}}^2}) \quad (3.12d)$$

which simplifies to

$$S_F^{\text{CSL}}(\omega) \approx \lambda_{\text{CSL}} \frac{16\pi \hbar^2 r_{\text{CSL}}^2}{m_0^2} \frac{\rho_0 m}{b_x} \times \begin{cases} 1 & \text{if } b_x \gg r_{\text{CSL}} \\ \frac{1}{2} & \text{if } b_x \approx r_{\text{CSL}} \\ \frac{b_x^2}{2r_{\text{CSL}}^2} & \text{if } b_x \ll r_{\text{CSL}}. \end{cases} \quad (3.13)$$

depending on the thickness b_x of the membrane.

3.3.3 CSL-induced torque on a torsion paddle:

We now consider a square plate ($b_x = b_z = b$) of mass $m = \rho_0 b^2 b_y$ rotated by 45° in the $x - z$ plane, and where the principal axis of rotation of the plate is its diagonal.

The structural factor is:

$$\tilde{\rho}_m(\mathbf{k}) = m \operatorname{sinc}\left(\frac{k_+b}{2}\right) \operatorname{sinc}\left(\frac{k_y b_y}{2}\right) \operatorname{sinc}\left(\frac{k_-b}{2}\right),$$

where $k_{\pm} = (k_x \pm k_z)/\sqrt{2}$.

$$\begin{aligned} S_{\tau}^{\text{CSL}}(\omega) &= 2\lambda_{\text{CSL}} \frac{\hbar^2 r_{\text{CSL}}^3 m^2}{\pi^{3/2} m_0^2} \int e^{-r_{\text{CSL}}^2 k^2} |(k_y \partial_{k_x} - k_x \partial_{k_y}) \tilde{\rho}_m(\mathbf{k})|^2 d^3 k = 2\lambda_{\text{CSL}} \frac{\hbar^2 r_{\text{CSL}}^3 m^2}{\pi^{3/2} m_0^2} \left(\right. \\ &\quad \int e^{-r_{\text{CSL}}^2 k_y^2 k_z^2} \operatorname{sinc}^2\left(\frac{k_y b_y}{2}\right) dk_y \int e^{-r_{\text{CSL}}^2 (k_x^2 + k_z^2)} \left(\partial_{k_x} \operatorname{sinc}\left(\frac{k_+b}{2}\right) \operatorname{sinc}\left(\frac{k_-b}{2}\right) \right)^2 dk_x dk_z \\ &\quad \left. - \int e^{-r_{\text{CSL}}^2 k_y^2} \left(\partial_{k_y} \operatorname{sinc}\left(\frac{k_y b_y}{2}\right) \right)^2 dk_y \int e^{-r_{\text{CSL}}^2 (k_x^2 + k_z^2)} k_x^2 \operatorname{sinc}^2\left(\frac{k_+b}{2}\right) \operatorname{sinc}^2\left(\frac{k_-b}{2}\right) dk_x dk_z \right) \end{aligned}$$

If $b \gg r_{\text{CSL}}$, we get (after some tedious algebra):

$$S_{\tau}^{\text{CSL}}(\omega) \approx \lambda_{\text{CSL}} \frac{16\pi \hbar^2 r_{\text{CSL}}^2 \rho_0 m}{m_0^2} \left(\frac{b^2}{b_y} - \frac{b_y^2}{b} \right).$$

If the plate is thin ($b_y \ll b$):

$$S_{\tau}^{\text{CSL}}(\omega) \approx \lambda_{\text{CSL}} \frac{16\pi \hbar^2 r_{\text{CSL}}^2 \rho_0 I_{zz}}{m_0^2 b_y}, \quad (3.14)$$

where $I_{zz} \approx mb^2/12$ is the moment of inertia of a thin, square plate about its diagonal axis.

Note that the expression for the CSL-induced torque on the square paddle is almost identical to the CSL-induced force on the membrane, with mass replaced by momentum of inertia.

3.3.4 Torsion pendulum as a torque sensor:

For testing CSL we consider a high- Q Si_3N_4 torsion micropendulum as described in Sec. 3.3.7. We here consider the torque sensitivity of this device, mirroring the analysis presented earlier for force sensing.

The net torque acting on the torsional paddle⁴ is (ignoring damping, which we will account for later):

$$\tau_{\text{net}}(t) = \tau_{\text{ext}}(t) - k_{\theta}\theta(t) = I\ddot{\theta}(t), \quad (3.15)$$

⁴We interchangeably use “torsion (micro)pendulum” and “torsion paddle”.

where $\tau_{\text{ext}}(t)$ is the net external torque acting on the paddle, k_θ is the torsional spring constant characterizing the stiffness of the torsion fiber, and I is the moment of inertia of the paddle. Rearranging gives the harmonic equation of motion:

$$\ddot{\theta}(t) + \omega_m^2 \theta(t) - \frac{\tau_{\text{ext}}(t)}{I} = 0, \quad (3.16)$$

where $\omega_m = \sqrt{k_\theta/I}$ is the natural frequency of the torsion pendulum.

We introduce damping in the frequency domain by apply the Fourier transform to Eq. 3.16, yielding

$$-\omega^2 \theta(\omega) + \omega_m^2 \theta(\omega) + \underbrace{i\omega\gamma_m(\omega)\theta(\omega)}_{\text{damping term}} - \frac{\tau_{\text{ext}}(\omega)}{I} = 0 \quad (3.17)$$

Or equivalently

$$\theta(\omega) = I^{-1} (-\omega^2 + \omega_m^2 + i\omega\gamma_m(\omega))^{-1} \tau_{\text{ext}}(\omega) \quad (3.18a)$$

$$\equiv \chi_{\theta\tau}(\omega) \tau_{\text{ext}}(\omega), \quad (3.18b)$$

where $\chi_{\theta\tau}(\omega)$ is the torque susceptibility of the torsional pendulum.

Re-expressing in terms of power spectral densities, and assuming structural damping gives

$$S_{\theta\theta}(\omega) = |\chi_{\theta\tau}(\omega)|^2 S_{\tau\tau}^{\text{ext}}(\omega) \quad (3.19a)$$

$$= ((\omega^2 - \omega_m^2)^2 + \omega_m^4/Q_m^2)^{-1} S_{\tau\tau}^{\text{ext}}(\omega). \quad (3.19b)$$

Equation 3.19 encapsulates the torque-sensing mechanism of our paddle, where the signal that is to be detected, $S_{\tau\tau}^{\text{ext}}(\omega)$, is coupled to our paddle's angular displacement, $S_{\theta\theta}(\omega)$.

3.3.5 Measurement sensitivity in the frequency domain:

Mirroring the analysis in section 1.3.1, we now consider the sensitivity of a torque measurement including readout noise. Towards this end we consider a measurement of the *angular* displacement of the torsion paddle including readout noise

$$\theta_{\text{meas}}(t) = \theta(t) + \theta_{\text{imp}}(t) \quad (3.20)$$

which in the Fourier domain becomes

$$\theta_{\text{meas}}(\omega) = \theta(\omega) + \theta_{\text{imp}}(\omega) \quad (3.21)$$

where θ_{imp} is the readout noise referred to an apparent displacement and

$$\theta(\omega) = \chi_{\theta\tau}(\omega) (\tau_{\text{CSL}}(\omega) + \tau_{\text{th}}(\omega) + \tau_{\text{ba}}(\omega)) \quad (3.22)$$

is the physical displacement produce by (hypothetical) CSL, thermal, and measurement back-action torque, respectively.

In PSD units, the total measurement signal is

$$S_{\theta\theta}^{\text{meas}}(\omega) = S_{\theta\theta}^{\text{CSL}}(\omega) + S_{\theta\theta}^{\text{th}}(\omega) + S_{\theta\theta}^{\text{ba}}(\omega) + S_{\theta\theta}^{\text{imp}}(\omega) \quad (3.23a)$$

$$= |\chi_{\theta\tau}(\omega)|^2 (S_{\tau\tau}^{\text{CSL}}(\omega) + S_{\tau\tau}^{\text{th}}(\omega) + S_{\tau\tau}^{\text{ba}}(\omega)) + S_{\theta\theta}^{\text{imp}}(\omega). \quad (3.23b)$$

where S_{τ}^{CSL} is the CSL torque from Eq. 3.14,

$$S_{\tau}^{\text{th}}(\omega) = 4k_{\text{B}}T\gamma_{\text{m}}(\omega)I, \quad (3.24)$$

is the thermal torque acting on the paddle (analogous to Eq. 1.25) and

$$S_{\tau}^{\text{ba}}(\omega) \geq \frac{\hbar^2}{S_{\theta}^{\text{imp}}(\omega)}, \quad (3.25)$$

is the back-action torque, which depends on the readout strategy. As described in [5], we employ an optical lever (Fig. ??) with imprecision:

$$S_{\theta}^{\text{imp}}(\omega) \gtrsim \frac{1}{w_0^2} \frac{\hbar c \lambda}{8P}, \quad (3.26)$$

where P is the optical power reflected from the paddle and w_0 is the spot size of the optical field.

Equating the CSL noise with the total measurement noise yields an upper bound on λ_{CSL} , i.e.

$$S_{\tau}^{\text{CSL}}(\omega) = \lambda_{\text{CSL}} \frac{16\pi\hbar^2 r_{\text{CSL}}^2 \rho_0 I}{m_0^2 b_y} \quad (3.27a)$$

$$\geq S_{\tau}^{\text{th}}(\omega) + S_{\tau}^{\text{ba}}(\omega) + |\chi_{\tau}(\omega)|^{-2} S_{\theta}^{\text{imp}}(\omega) \quad (3.27b)$$

$$\implies \lambda_{\text{CSL}}(\omega) \frac{m_0^2}{16\pi\hbar^2 r_{\text{CSL}}^2 \rho_0 I} b_y \left(S_{\tau}^{\text{th}}(\omega) + S_{\tau}^{\text{ba}}(\omega) + |\chi_{\theta\tau}(\omega)|^{-2} S_{\theta}^{\text{imp}}(\omega) \right) \quad (3.27c)$$

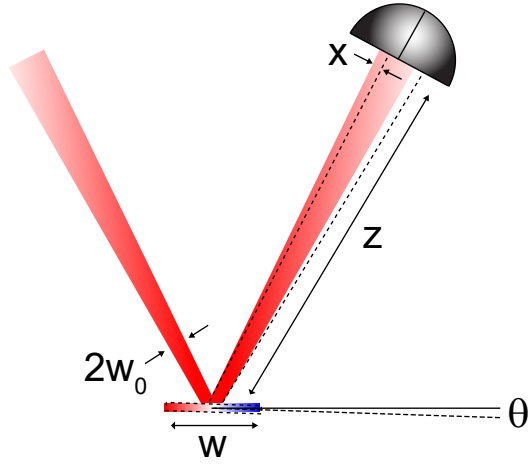


Figure 3.1: **Schematic of optical lever measurement** (taken with permission from [5]): A Gaussian laser beam with a waist, w_0 , is reflected off the torsion paddle and its deflection is monitored using a split-photodiode a distance, z , away. Angular displacement, θ , of the torsion paddle produces a displacement of $x = 2\theta z$ of the optical beam on the split photodiode.

3.3.6 Thermal-Noise-Limited CSL constraints

Thermal noise sets an ultimate limit on the sensitivity to CSL noise, for both torsion pendula and membranes. In both cases, it turns out that:

$$\lambda_{\text{CSL}}^{\text{max}}(\omega_{\text{m}}) \propto \frac{b\omega_{\text{m}}T}{\rho Q_{\text{m}}},$$

where b is the thickness of the paddle (b_y) or membrane (b_x). We consider the two cases individually below:

a) Torsion paddle: Comparing the CSL torque (Eq. 3.14) to the thermal torque (Eq. 3.25) yields

$$\lambda_{\text{CSL}}^{\text{max}}(\omega) = \frac{m_0^2 b_y}{16\pi\hbar^2 r_{\text{CSL}}^2 \rho_{\text{m}} I_{zz}} S_{\tau}^{\text{th}}(\omega) = \frac{b_y \omega_{\text{m}} T}{\rho_0 Q_{\text{m}}} \frac{k_B m_0^2}{4\pi\hbar^2 r_{\text{CSL}}^2} \frac{\gamma_{\text{m}}(\omega)}{\gamma_{\text{m}}(\omega_{\text{m}})}. \quad (3.28)$$

b) Nanomembrane: Comparing the CSL force (Eq. 3.13) with the thermal force (Eq. 1.25) and assuming ideal thickness $b_x \approx r_{\text{CSL}}$ yields

$$\lambda_{\text{CSL}}^{\text{max}}(\omega) \approx \frac{m_0^2}{8\pi\hbar^2 r_{\text{CSL}} \rho_0 m} S_F^{\text{th}}(\omega) \approx \frac{b_x \omega_{\text{m}}}{\rho_0 Q_{\text{m}}} \frac{k_B T m_0^2}{2\pi\hbar^2 r_{\text{CSL}}^2} \frac{\gamma_{\text{m}}(\omega)}{\gamma_{\text{m}}(\omega_{\text{m}})} \quad (3.29)$$

3.3.7 Torsion micropendulum device

In this section, we will discuss a Si_3N_4 torsion micropendulum fabricated and read out with deflectometry measurements in our lab [5].

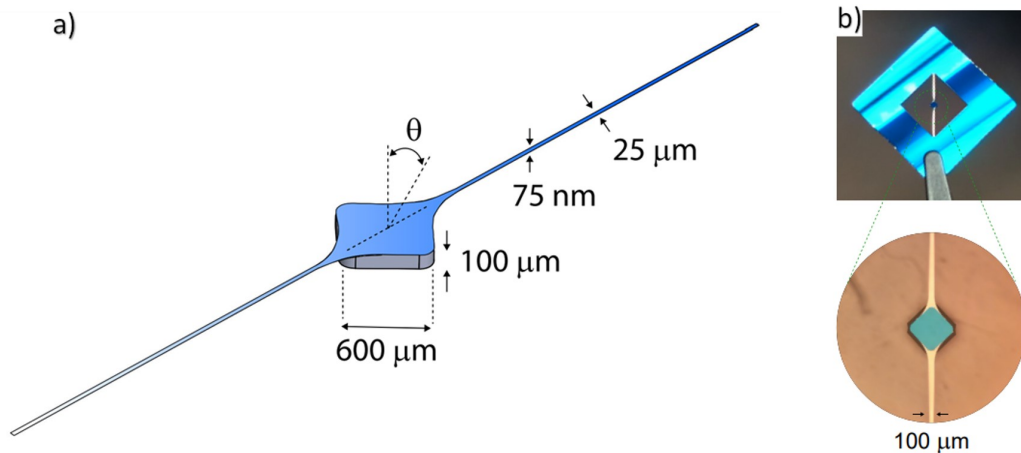


Figure 3.2: (a) Geometry and (b) micrograph of Si_3N_4 torsion micropendulum, taken with permission from [5]

As shown in Fig. 3.2, the device consists of a rigid, $100\ \mu\text{m}$ thick, $600\ \mu\text{m} \times 600\ \mu\text{m}$ Si pad (the torsion paddle) suspended from a $75\ \text{nm}$ thick, $25\ \mu\text{m}$ wide Si_3N_4 , $7\ \text{mm}$ long nanoribbon (the torsion fiber).⁵

As described in [5], a powerful feature of Si_3N_4 nanoribbons with respect to inertial sensing is their ability to be mass-loaded without reduction in their torsional Q -factors. In-vacuum measurements revealed

⁵It is interesting to note that the torsion micropendulum is made from the trampoline device used for the dark matter proposal, by two of the four Si_3N_4 tethers while etching.

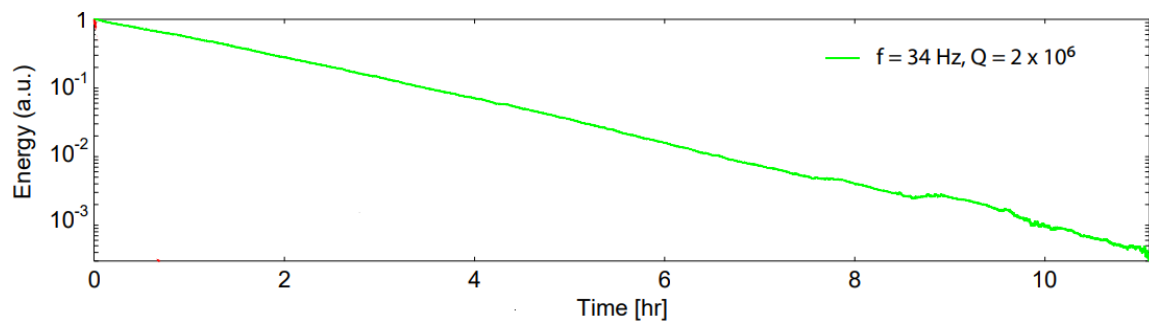


Figure 3.3: [5] Ringdown of a $\omega_m = 2\pi \cdot 40\ \text{Hz}$, $Q_m = 2 \times 10^6$ Si_3N_4 torsion micropendulum. This device was used for CSL constraints shown in Fig. 4.2

a 1000-fold drop in the fundamental torsion resonance frequency of the ribbons, from 40 kHz to 34 Hz, corresponding to a million-fold increase in moment of inertia. Despite this substantial mass-loading, ringdown measurements revealed an increased quality factor of $Q_m \approx 2.5 \times 10^6$, relative to the unloaded ribbon's, $Q_m \approx 1.5 \times 10^6$. (This increase in Q is due to the lossless gravitational restoring torque of the paddle.)

Chapter 4

RESULTS AND DISCUSSION

In Figure 4.1 and 4.2 we present predicted DM constraints and estimated CSL constraints based on the room temperature noise floor of our TOM

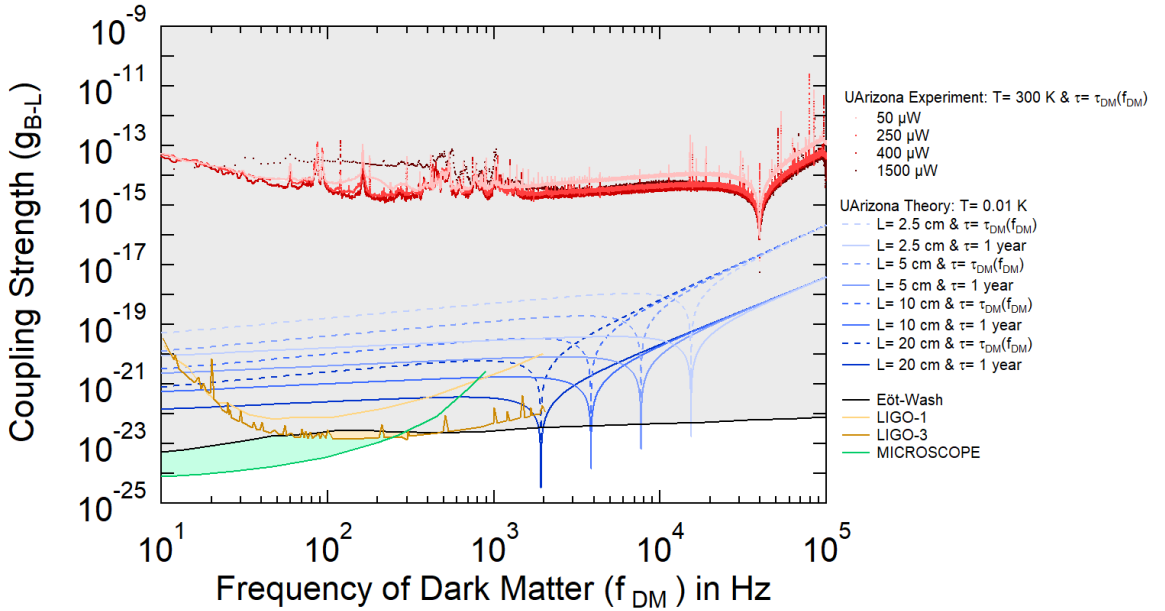


Figure 4.1: **Contemporary and predicted constraints on $B - L$ dark photon coupling:** Dashed-blue and solid-blue curves are models for the acceleration sensitivity of four different membranes, expressed as minimum DM coupling strength, g_{B-L} , for a measurement time equal to the DM coherence time ($\tau_{\text{DM}} = 2Q_{\text{DM}}/\omega_{\text{DM}}$) and one year, respectively. Each model assumes $Q_{\text{m}} = 10^9$, an operating temperature of $T = 10$ mK, a displacement sensitivity of 2×10^{-17} m/ $\sqrt{\text{Hz}}$, and a suppression factor of $f_{12} = 0.068$ relative to a Germanium (Ge) reference mass. It is evident that larger membranes yield stronger constraints. The black, yellow/brown, and green plots are bounds set by the Eöt-Wash [32] experiments, LIGO-1 [33]/LIGO-3 [34], and MICROSCOPE [35], respectively. The plots in various shades of red are hypothetical bounds for our TOM accelerometer based on the room temperature noise floors in Fig. 2.6, assuming a measurement time equal to the DM coherence time and also assuming $f_{12} = 0.068$ by placing the device atop a Ge substrate as shown in Fig. 2.3.

accelerometer and torsion micropendulum (read out with an optical lever [5]), respectively. Details are provided in the captions and in further discussion given below.

DM constraints. Blue and red curves in Fig. 4.1 are $B - L$ dark photon coupling bounds inferred from theoretical and experimental (see Fig. 2.6) sensitivities of a membrane accelerometer. The blue models were generated using Mathematica assuming parameters discussed in the caption. We used the imprecision noise model $S_{xx}^{\text{imp}} = \pi \hbar c \lambda / (64 \mathcal{F}^2 P)$ with laser wavelength $\lambda = 1 \mu\text{m}$, cavity finesse $\mathcal{F} = 100$, and optical power $P = 0.3 \text{ mW}$. For the experimental curves, inferred from the noise floors of the room temperature TOM accelerometer in Fig. 2.6, we would like to emphasize again that the bounds are hypothetical, as they assume the device is fixed to a Ge-reference mass as shown in Fig. 2.3.

CSL constraints - torsion micropendulum: The CSL constraint drawn from optical lever readout of our torsion micropendulum is shown as a purple, dotted curve in Fig. 4.2. The curve was obtained by dividing the optical lever measurement (calibrated by translating the split photodetector by a known amount [5]) by the susceptibility of the torsion pendulum inferred from ringdown measurement in Fig. 3.3. The dispersive feature at the mechanical resonance frequency ($\sim 40 \text{ Hz}$) is caused by a mismatch between the actual and modeled resonance frequency due by drift. Since the mechanical linewidth of the micropendulum is only $\gamma_m \approx 2\pi \cdot 20 \mu\text{Hz}$, this artefact is difficult to avoid. We note that the measurement shown, the device is suspended from a custom vibration isolation stage atop our optical table.

CSL constraints - nanomembrane: CSL constraints drawn from the noise floor of our room temperature TOM accelerometer are shown as pink dashed lines in Fig. 4.2. These curves were obtained by first converting the acceleration noise spectra Fig. 2.6 to force noise by multiplying by the effective mass of the trampoline ($m \approx 12 \text{ ng}$), then equating the force noise to the CSL noise (Eq. 3.13) using a membrane thickness of $b_x = 75 \text{ nm}$.

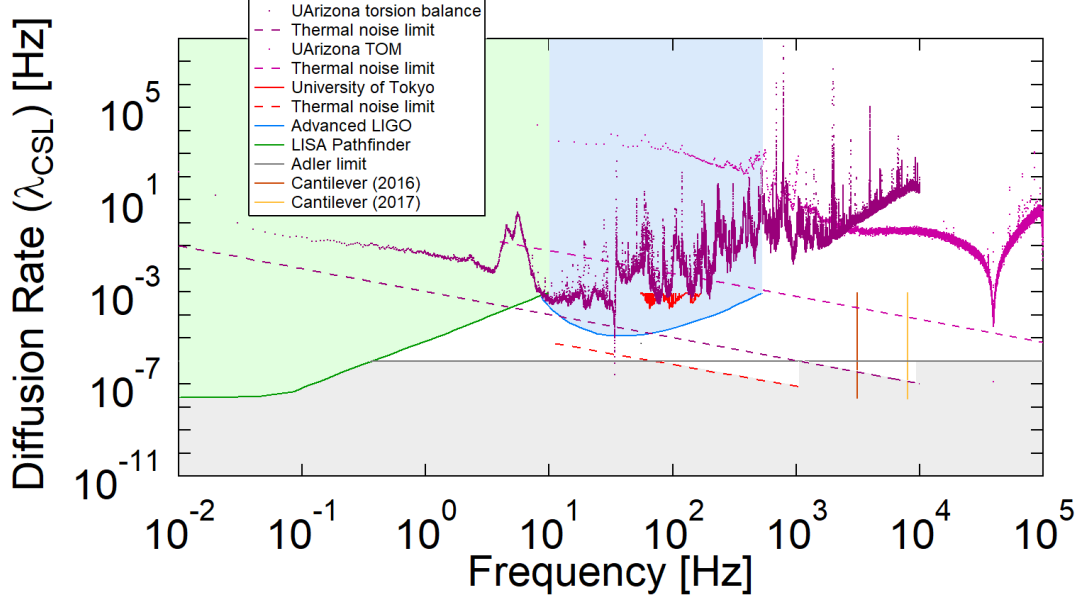


Figure 4.2: **Landscape of the CSL diffusion rate bounds by various mechanical experiments [24]:** The purple and pink dotted plots refer to the diffusion rate bounds inferred from our torsional balance and TOM experiment, respectively; while the purple and pink dashed plots refer to their respective CSL bounds, if they were limited by thermal noise that follows structural damping. At higher frequencies, we can see that TOM sets more stringent bounds as compared to the torsion balance. The gray region represents the range of diffusion parameters yet to be tested [36]. Resonant thermal-noise measurements using cryogenic cantilevers [29, 37] exclude a narrow range of parameters at 1-10 kHz. Advanced LIGO’s sensitivity does not yet broach this interesting region [38], while LISA Path Finder does exclude swaths at low frequency [39]. The red region represents the optomechanical torsion pendulum experiment by Kentaro Komori et al. [24] that recorded a torque sensitivity of $20 \text{ aNm}/\sqrt{\text{Hz}}$, while the red dashed line corresponds to the experiment limited by thermal torque noise that follows structural damping.

Chapter 5

CONCLUSION AND OUTLOOK

By combining quantum-limited displacement readout with cryogenic operating temperatures, the sensitivity of our DM detector is expected to exceed current bounds set by the Eöt-Wash experiments, in measurement time of minutes, over a fractional bandwidth of $\sim 0.1\%$ in the mass range, $10^{-11} - 10^{-10} \text{ eV}/c^2$. It is also possible to implement scanning techniques [11] that could broaden the bandwidth of our detector to more than an octave. Looking forward, we anticipate that a variety of optomechanical accelerometer platforms can perform similarly as vector ULDM detectors. Optically or magnetically levitated test masses seem particularly promising, as in addition to high $Q_0 \times m$ factors, they can be frequency scanned over a wide bandwidth [40, 41, 42]. Our ULDM analysis assumes that TOM’s mechanical resonance frequency is matched to the DM signal frequency, which is very unlikely to be the case, in reality. To circumvent this “needle in a haystack” problem, array-based networks are called for. Collaboration and teamwork is highly desirable, where each individual experiment can focus on a particular frequency range.

For both, our DM and CSL detection experiments, we plan to carry out measurements at cryogenic temperatures, using a 4K continuous flow cryostat and, later, a sub-100-mK dilution refrigerator. These will lead to much dramatically improved constraints due to reduction of thermal noise; however the bandwidth will remain limited by imprecision noise. By introducing a photonic crystal, we can improve the reflectivity ($\sim 99\%$) and finesse inside the cavity, thus decreasing the imprecision shot noise. We also are trying to leverage dissipation dilution for increasing the mechanical Q of the system. Ultimately, we target reducing thermal noise to the level that only radiation pressure and imprecision shot noise dominate, enabling us to explore the Standard Quantum Limit, laser cooling to the motional ground state, and other possible quantum effects that are not typically observed on macro-scale objects.

BIBLIOGRAPHY

- [1] Markus Aspelmeyer, Tobias J. Kippenberg, and Florian Marquardt. “Cavity optomechanics”. In: *Rev. Mod. Phys.* 86 (4 Dec. 2014), pp. 1391–1452. DOI: [10.1103/RevModPhys.86.1391](https://doi.org/10.1103/RevModPhys.86.1391). URL: <https://link.aps.org/doi/10.1103/RevModPhys.86.1391>.
- [2] John D Teufel et al. “Nanomechanical motion measured with an imprecision below that at the standard quantum limit”. In: *Nature nanotechnology* 4.12 (2009), pp. 820–823. URL: <https://www.nature.com/articles/nnano.2009.343>.
- [3] Christian M. Pluchar et al. “Towards cavity-free ground-state cooling of an acoustic-frequency silicon nitride membrane”. In: *Appl. Opt.* 59.22 (Aug. 2020), G107–G111. DOI: [10.1364/AO.394388](https://doi.org/10.1364/AO.394388). URL: <http://opg.optica.org/ao/abstract.cfm?URI=ao-59-22-G107>.
- [4] Francesco Fogliano et al. “Ultrasensitive nano-optomechanical force sensor operated at dilution temperatures”. In: *Nature Communications* 12.1 (2021), pp. 1–8. URL: <https://www.nature.com/articles/s41467-021-24318-y>.
- [5] Jon R. Pratt et al. “Nanoscale torsional dissipation dilution for quantum experiments and precision measurement”. In: 2021. URL: <https://arxiv.org/abs/2112.08350>.
- [6] Dalziel J. Wilson. “Cavity Optomechanics with High Stress Silicon Nitride Films”. PhD thesis. <https://thesis.library.caltech.edu/7162/>: California Institute of Technology, 2012.
- [7] Peter R. Saulson. “Thermal noise in mechanical experiments”. In: *Phys. Rev. D* 42 (8 Oct. 1990), pp. 2437–2445. DOI: [10.1103/PhysRevD.42.2437](https://doi.org/10.1103/PhysRevD.42.2437). URL: <https://link.aps.org/doi/10.1103/PhysRevD.42.2437>.
- [8] David J.E. Marsh. “Axion cosmology”. In: *Physics Reports* 643 (2016), pp. 1–79. ISSN: 0370-1573. DOI: <https://doi.org/10.1016/j.physrep.2016.06.005>. URL: <https://www.sciencedirect.com/science/article/pii/S0370157316301557>.
- [9] Katherine Freese, Mariangela Lisanti, and Christopher Savage. “Colloquium: Annual modulation of dark matter”. In: *Rev. Mod. Phys.* 85 (4 Nov. 2013), pp. 1561–1581. DOI: [10.1103/RevModPhys.85.1561](https://doi.org/10.1103/RevModPhys.85.1561). URL: <https://link.aps.org/doi/10.1103/RevModPhys.85.1561>.
- [10] M. Tanabashi et al. (Particle Data Group). “Review of Particle Physics”. In: *Phys. Rev. D* 98 (3 Aug. 2018), p. 030001. DOI: [10.1103/PhysRevD.98.030001](https://doi.org/10.1103/PhysRevD.98.030001). URL: <https://link.aps.org/doi/10.1103/PhysRevD.98.030001>.

- [11] Jack Manley et al. “Searching for Vector Dark Matter with an Optomechanical Accelerometer”. In: *Phys. Rev. Lett.* 126 (6 Feb. 2021), p. 061301. DOI: [10.1103/PhysRevLett.126.061301](https://doi.org/10.1103/PhysRevLett.126.061301). URL: <https://link.aps.org/doi/10.1103/PhysRevLett.126.061301>.
- [12] Peter W. Graham et al. “Dark matter direct detection with accelerometers”. In: *Phys. Rev. D* 93 (7 Apr. 2016), p. 075029. DOI: [10.1103/PhysRevD.93.075029](https://doi.org/10.1103/PhysRevD.93.075029). URL: <https://link.aps.org/doi/10.1103/PhysRevD.93.075029>.
- [13] Dmitry Budker et al. “Proposal for a Cosmic Axion Spin Precession Experiment (CASPER)”. In: *Phys. Rev. X* 4 (2 May 2014), p. 021030. DOI: [10.1103/PhysRevX.4.021030](https://doi.org/10.1103/PhysRevX.4.021030). URL: <https://link.aps.org/doi/10.1103/PhysRevX.4.021030>.
- [14] Mitul D. Chowdhury, Aman R. Agrawal, and Dalziel J. Wilson. “Membrane-based Optomechanical Accelerometry”. In preparation.
- [15] Angelo Bassi. “Models of spontaneous wave function collapse: what they are, and how they can be tested”. In: *Journal of Physics: Conference Series* 701 (Mar. 2016), p. 012012. DOI: [10.1088/1742-6596/701/1/012012](https://doi.org/10.1088/1742-6596/701/1/012012). URL: <https://doi.org/10.1088/1742-6596/701/1/012012>.
- [16] Angelo Bassi and GianCarlo Ghirardi. “Dynamical reduction models”. In: *Physics Reports* 379.5 (2003), pp. 257–426. ISSN: 0370-1573. DOI: [https://doi.org/10.1016/S0370-1573\(03\)00103-0](https://doi.org/10.1016/S0370-1573(03)00103-0). URL: <https://www.sciencedirect.com/science/article/pii/S0370157303001030>.
- [17] Gian Carlo Ghirardi, Philip Pearle, and Alberto Rimini. “Markov processes in Hilbert space and continuous spontaneous localization of systems of identical particles”. In: *Phys. Rev. A* 42 (1 July 1990), pp. 78–89. DOI: [10.1103/PhysRevA.42.78](https://doi.org/10.1103/PhysRevA.42.78). URL: <https://link.aps.org/doi/10.1103/PhysRevA.42.78>.
- [18] G. C. Ghirardi, A. Rimini, and T. Weber. “Unified dynamics for microscopic and macroscopic systems”. In: *Phys. Rev. D* 34 (2 July 1986), pp. 470–491. DOI: [10.1103/PhysRevD.34.470](https://doi.org/10.1103/PhysRevD.34.470). URL: <https://link.aps.org/doi/10.1103/PhysRevD.34.470>.
- [19] Angelo Bassi et al. “Models of wave-function collapse, underlying theories, and experimental tests”. In: *Rev. Mod. Phys.* 85 (2 Apr. 2013), pp. 471–527. DOI: [10.1103/RevModPhys.85.471](https://doi.org/10.1103/RevModPhys.85.471). URL: <https://link.aps.org/doi/10.1103/RevModPhys.85.471>.
- [20] Philip Pearle. “Combining stochastic dynamical state-vector reduction with spontaneous localization”. In: *Phys. Rev. A* 39 (5 Mar. 1989), pp. 2277–2289. DOI: [10.1103/PhysRevA.39.2277](https://doi.org/10.1103/PhysRevA.39.2277). URL: <https://link.aps.org/doi/10.1103/PhysRevA.39.2277>.

- [21] Marko Toroš, Giulio Gasbarri, and Angelo Bassi. “Colored and dissipative continuous spontaneous localization model and bounds from matter-wave interferometry”. In: *Physics Letters A* 381.47 (2017), pp. 3921–3927. ISSN: 0375-9601. DOI: <https://doi.org/10.1016/j.physleta.2017.10.002>. URL: <https://www.sciencedirect.com/science/article/pii/S0375960117309465>.
- [22] A. Bassi and S. Donadi. “Spontaneous photon emission from a non-relativistic free charged particle in collapse models: A case study”. In: *Physics Letters A* 378.10 (2014), pp. 761–765. ISSN: 0375-9601. DOI: <https://doi.org/10.1016/j.physleta.2014.01.002>. URL: <https://www.sciencedirect.com/science/article/pii/S0375960114000073>.
- [23] Stephen L. Adler and Andrea Vinante. “Bulk heating effects as tests for collapse models”. In: *Phys. Rev. A* 97 (5 May 2018), p. 052119. DOI: [10.1103/PhysRevA.97.052119](https://doi.org/10.1103/PhysRevA.97.052119). URL: <https://link.aps.org/doi/10.1103/PhysRevA.97.052119>.
- [24] Kentaro Komori et al. “Attonewton-meter torque sensing with a macroscopic optomechanical torsion pendulum”. In: *Phys. Rev. A* 101 (1 Jan. 2020), p. 011802. DOI: [10.1103/PhysRevA.101.011802](https://doi.org/10.1103/PhysRevA.101.011802). URL: <https://link.aps.org/doi/10.1103/PhysRevA.101.011802>.
- [25] Matteo Carlesso et al. “Non-interferometric test of the continuous spontaneous localization model based on rotational optomechanics”. In: *New Journal of Physics* 20.8 (Aug. 2018), p. 083022. DOI: [10.1088/1367-2630/aad863](https://doi.org/10.1088/1367-2630/aad863). URL: <https://doi.org/10.1088/1367-2630/aad863>.
- [26] Kristian Piscicchia et al. “CSL Collapse Model Mapped with the Spontaneous Radiation”. In: *Entropy* 19.7 (2017). ISSN: 1099-4300. DOI: [10.3390/e19070319](https://doi.org/10.3390/e19070319). URL: <https://www.mdpi.com/1099-4300/19/7/319>.
- [27] Stefan Nimmrichter, Klaus Hornberger, and Klemens Hammerer. “Optomechanical Sensing of Spontaneous Wave-Function Collapse”. In: *Phys. Rev. Lett.* 113 (2 July 2014), p. 020405. DOI: [10.1103/PhysRevLett.113.020405](https://doi.org/10.1103/PhysRevLett.113.020405). URL: <https://link.aps.org/doi/10.1103/PhysRevLett.113.020405>.
- [28] M. Bahrami et al. “Proposal for a Noninterferometric Test of Collapse Models in Optomechanical Systems”. In: *Phys. Rev. Lett.* 112 (21 May 2014), p. 210404. DOI: [10.1103/PhysRevLett.112.210404](https://doi.org/10.1103/PhysRevLett.112.210404). URL: <https://link.aps.org/doi/10.1103/PhysRevLett.112.210404>.
- [29] A. Vinante et al. “Upper Bounds on Spontaneous Wave-Function Collapse Models Using Millikelvin-Cooled Nanocantilevers”. In: *Phys. Rev. Lett.* 116 (9 Mar. 2016), p. 090402. DOI: [10.1103/PhysRevLett.116.090402](https://doi.org/10.1103/PhysRevLett.116.090402). URL: <https://link.aps.org/doi/10.1103/PhysRevLett.116.090402>.

- [30] Lajos Diósi. “Testing Spontaneous Wave-Function Collapse Models on Classical Mechanical Oscillators”. In: *Phys. Rev. Lett.* 114 (5 Feb. 2015), p. 050403. DOI: [10.1103/PhysRevLett.114.050403](https://doi.org/10.1103/PhysRevLett.114.050403). URL: <https://link.aps.org/doi/10.1103/PhysRevLett.114.050403>.
- [31] Björn Schrinnski, Benjamin A. Stickler, and Klaus Hornberger. “Collapse-induced orientational localization of rigid rotors [Invited]”. In: *J. Opt. Soc. Am. B* 34.6 (June 2017), pp. C1–C7. DOI: [10.1364/JOSAB.34.0000C1](https://doi.org/10.1364/JOSAB.34.0000C1). URL: <http://opg.optica.org/josab/abstract.cfm?URI=josab-34-6-C1>.
- [32] S. Schlamminger et al. “Test of the Equivalence Principle Using a Rotating Torsion Balance”. In: *Phys. Rev. Lett.* 100 (4 Jan. 2008), p. 041101. DOI: [10.1103/PhysRevLett.100.041101](https://doi.org/10.1103/PhysRevLett.100.041101). URL: <https://link.aps.org/doi/10.1103/PhysRevLett.100.041101>.
- [33] Huai-Ke Guo et al. “Searching for dark photon dark matter in LIGO O1 data”. In: *Communications Physics* 2.1 (2019), pp. 1–7.
- [34] R Abbott et al. “Constraints on dark photon dark matter using data from LIGO’s and Virgo’s third observing run”. In: *Physical review D* 105.6 (2022), p. 063030.
- [35] Pierre Touboul et al. “MICROSCOPE Mission: First Results of a Space Test of the Equivalence Principle”. In: *Phys. Rev. Lett.* 119 (23 Dec. 2017), p. 231101. DOI: [10.1103/PhysRevLett.119.231101](https://doi.org/10.1103/PhysRevLett.119.231101). URL: <https://link.aps.org/doi/10.1103/PhysRevLett.119.231101>.
- [36] Stephen L Adler. “Lower and upper bounds on CSL parameters from latent image formation and IGM heating”. In: *Journal of Physics A: Mathematical and Theoretical* 40.12 (2007), p. 2935. URL: <https://iopscience.iop.org/article/10.1088/1751-8113/40/12/S03/meta>.
- [37] A. Vinante et al. “Improved Noninterferometric Test of Collapse Models Using Ultracold Cantilevers”. In: *Phys. Rev. Lett.* 119 (11 Sept. 2017), p. 110401. DOI: [10.1103/PhysRevLett.119.110401](https://doi.org/10.1103/PhysRevLett.119.110401). URL: <https://link.aps.org/doi/10.1103/PhysRevLett.119.110401>.
- [38] Matteo Carlesso et al. “Experimental bounds on collapse models from gravitational wave detectors”. In: *Phys. Rev. D* 94 (12 Dec. 2016), p. 124036. DOI: [10.1103/PhysRevD.94.124036](https://doi.org/10.1103/PhysRevD.94.124036). URL: <https://link.aps.org/doi/10.1103/PhysRevD.94.124036>.
- [39] Bassam Helou et al. “LISA pathfinder appreciably constrains collapse models”. In: *Phys. Rev. D* 95 (8 Apr. 2017), p. 084054. DOI: [10.1103/PhysRevD.95.084054](https://doi.org/10.1103/PhysRevD.95.084054). URL: <https://link.aps.org/doi/10.1103/PhysRevD.95.084054>.

- [40] Fernando Monteiro et al. “Optical levitation of 10-ng spheres with nano- g acceleration sensitivity”. In: *Phys. Rev. A* 96 (6 Dec. 2017), p. 063841. DOI: [10.1103/PhysRevA.96.063841](https://doi.org/10.1103/PhysRevA.96.063841). URL: <https://link.aps.org/doi/10.1103/PhysRevA.96.063841>.
- [41] Charles W. Lewandowski et al. “High-Sensitivity Accelerometry with a Feedback Cooled Magnetically Levitated Microsphere”. In: *Phys. Rev. Applied* 15 (1 Jan. 2021), p. 014050. DOI: [10.1103/PhysRevApplied.15.014050](https://doi.org/10.1103/PhysRevApplied.15.014050). URL: <https://link.aps.org/doi/10.1103/PhysRevApplied.15.014050>.
- [42] Chris Timberlake et al. “Acceleration sensing with magnetically levitated oscillators above a superconductor”. In: *Applied Physics Letters* 115.22 (2019), p. 224101. URL: <https://aip.scitation.org/doi/abs/10.1063/1.5129145>.